

**A Look at Convective Atmospheric Boundary  
Layer Entrainment Scales using Large Eddy  
Simulation**

by

Niamh Chaparro

A THESIS SUBMITTED IN PARTIAL FULFILLMENT  
OF THE REQUIREMENTS FOR THE DEGREE OF

**MSc**

in

THE FACULTY OF GRADUATE STUDIES  
(Earth, Ocean and Atmospheric Sciences)

The University Of British Columbia  
(Vancouver)

*missing submission month    missing submission year*

© Niamh Chaparro,    *missing submission year*

# Table of Contents

<b>Table of Contents . . . . .</b>	<b>ii</b>
<b>List of Figures . . . . .</b>	<b>iv</b>
<b>Glossary . . . . .</b>	<b>viii</b>
<b>1 Introduction . . . . .</b>	<b>1</b>
1.1 Motivation . . . . .	1
1.2 Relevant Background . . . . .	2
1.2.1 The Convective Boundary Layer (CBL) . . . . .	2
1.2.2 CBL Height ( $h$ ) . . . . .	5
1.2.3 CBL Growth by Entrainment . . . . .	7
1.2.4 The CBL Entrainment Layer (EL) . . . . .	7
1.2.5 Modelling the CBL and EL . . . . .	9
1.2.6 Scales and Scaling Relations of the CBL and EL . . . . .	13
1.3 Research Questions . . . . .	19
1.4 Approach to Research Questions . . . . .	20
<b>2 Results . . . . .</b>	<b>24</b>
2.1 Description of Runs . . . . .	24
2.2 Relevant Definitions . . . . .	25
2.3 Verifying the Model Output . . . . .	27
2.3.1 Time till well-mixed . . . . .	27
2.3.2 FFT Energy Spectra . . . . .	31
2.3.3 Ensemble and horizontally averaged vertical Potential Temperature $\bar{\theta}$ and Heat Flux profiles $\overline{w'\theta'}$ . . . . .	32

2.3.4	Visualization of Structures Within the Entrainment Layer	35
2.4	Local Mixed Layer Heights ( $h_0^l$ )	38
2.5	Flux Quadrants	43
2.6	$h$ and $\Delta h$ based on Average Profiles	53
2.6.1	$\frac{\Delta h}{h}$ vs $Ri^b$	53
2.6.2	$\frac{w_e}{w^*}$ vs $Ri^{-1}$	54
<b>References</b>		<b>64</b>
<b>A Appendices</b>		<b>67</b>
A.1	Potential Temperature: $\theta$	67
A.2	Second Law of Thermodynamics	68
A.3	Reynolds Decomposition and Simplification of Conservation of Enthalpy (or Entropy) for a dry Atmosphere	68
A.4	Reynolds averaged Turbulence Kinetic Energy Equation	69

# List of Figures

Figure 1.1 Lidar backscatter image of the CBL from DuPont et al. 1994. The horizontal distance between the two peaks corresponds to approximately 1700 meters. . . . .	3
Figure 1.2 Flow visualization from Sullivan et al. 1998 showing a modelled CBL thermal enveloping FA air. . . . .	4
Figure 1.3 Idealized vertical average profiles for a dry CBL in the absence of large scale winds or subsidence. (a) $\bar{\theta}_{ML}$ is the average mixed layer potential temperature. $h$ is the height of maximum gradient in the $\bar{\theta}$ profile. $\bar{\theta}_0$ (dotted line) is the initial $\bar{\theta}$ profile which has a slope $\gamma$ . The mixed layer, entrainment layer and free atmosphere are denoted ML, EL and FA respectively. (b) $\overline{w'\theta'}$ is the average surface turbulent heat flux. The EL limits (dashed lines) enclose the region of negative $\overline{w'\theta'}$ . . . . .	5
Figure 1.4 Simplified version of Figure 1.3 such that the EL is infinitesimally thin. (a) $h$ is the height of the inversion and $\delta\theta$ the corresponding temperature jump, that is, the difference between $\bar{\theta}_{ML}$ and $\bar{\theta}_0(h)$ . This is different, although related, to the jump across the EL in Figure 1.3 $\Delta\theta$ . (b) The $\overline{w'\theta'}$ profile is linear and decreasing until it reaches a maximum negative value at $h$ of $-.2(\overline{w'\theta'})_s$ . Here there is a discontinuity as it jumps to zero. . . . .	10
Figure 1.5 Height definitions based on the average vertical profiles. $\theta_0$ is the initial potential temperature. . . . .	23

Figure 2.1	CBL height and EL limit definitions based on the $\frac{\partial \bar{\theta}}{\partial z}$ and $\overline{w'\theta'}$ profiles. . . . .	26
Figure 2.2	Plots of scaled time vs time for all runs. Scaled time is based on the convective time scale and can be thought of as the number of times an eddie has reached the top of the CBL. . . . .	28
Figure 2.3	Vertical profiles of the ensemble and horizontally averaged potential temperature ( $\bar{\theta}$ ), its vertical gradient ( $\frac{\partial \bar{\theta}}{\partial z}$ ) and heat flux ( $\overline{w'\theta'}$ ) for the 100/5 run . . . . .	29
Figure 2.4	$\overline{w'\theta'}$ and scaled $\overline{w'\theta'}$ vs scaled height for the 100/5 run . . . . .	29
Figure 2.5	(a) $\sqrt{w'^2}$ and scaled $\sqrt{w'^2}$ vs scaled height for the 150/10 run, (b) $\sqrt{u'^2}$ and scaled $\sqrt{u'^2}$ vs scaled height for the 150/10 run . . . . .	30
Figure 2.6	Scalar FFT energy vs wavenumber ( $k = \sqrt{k_x^2 + k_y^2}$ ) for the 60/2.5 run at 2 hours. $E(k)$ is $E(k_x, k_y)$ integrated around circles of radius $k$ . $E(k_x, k_y)$ is the total integrated energy over the 2D domain. $k_x$ and $k_y$ are number of waves per domain length. . . . .	31
Figure 2.7	$\bar{\theta}$ profiles at 2 hours . . . . .	33
Figure 2.8	Scaled $\overline{w'\theta'_s}$ profiles at 2 hours . . . . .	34
Figure 2.9	$\theta'$ (left) and $w'$ (right) at 2 hours at $h_0$ (a,d), $h$ (c,e) and $h_1$ (d,f) . . . . .	36
Figure 2.10	$\theta'$ (left) and $w'$ (right) at 2 hours at $h_0$ (a,d), $h$ (b,e) and $h_1$ (c,f) . . . . .	37
Figure 2.11	Local vertical $\theta$ profiles with 3-line fit for the 60/2.5 (a) and 150/10 (b) runs at points where $h_0^l$ is high. . . . .	39
Figure 2.12	Local vertical $\theta$ profiles with 3-line fit for the 60/2.5 (a) and 150/10 (b) runs at points where $h_0^l$ is low. . . . .	39
Figure 2.13	$\theta'$ (a,d), $w'$ (b,e) at $h_1$ (c,f) and local ML height $h_0^l$ at 2 hours for 60/2.5 (left) and 150/10 (right) runs . . . . .	40
Figure 2.14	Histograms of $h_0^l$ for $\overline{w'\theta'_s} = 150$ to 60( $W/m^2$ ) (a to c) and $\gamma = 10$ to 2.5( $K/Km$ ) (c to g) at 5 hours . . . . .	41

Figure 2.15 PDFs of $\frac{h_0^l}{h}$ for $\overline{w'\theta'_s} = 150$ to $60(W/m^2)$ (a to c) and $\gamma = 10$ to $2.5(K/Km)$ (c to g) at 5 hours . . . . .	42
Figure 2.16 Scaled $\overline{w'\theta'}$ quadrant profiles at 5 hours for the 60/2.5 (a) and 150/10 (b) run . . . . .	44
Figure 2.17 $\overline{w'\theta'}$ quadrants at $h_0$ for $w'\theta' = 150 - 60(W/m^2)$ (top- bottom) and $\gamma = 10 - 2.5(K/Km)$ (left-right) at 5 hours . . . . .	45
Figure 2.18 $\overline{w'\theta'}$ quadrants at $h_0$ for $w'\theta' = 150 - 60(W/m^2)$ (top- bottom) and $\gamma = 10 - 2.5(K/Km)$ (left-right) at 5 hours . . . . .	46
Figure 2.19 $\overline{w'\theta'}$ quadrants at $h$ for $w'\theta' = 150 - 60(W/m^2)$ (top - bottom) and $\gamma = 10 - 2.5(K/Km)$ (left - right) at 5 hours . . . . .	47
Figure 2.20 $\overline{w'\theta'}$ quadrants at $h$ for $w'\theta' = 150 - 60(W/m^2)$ (top - bottom) and $\gamma = 10 - 2.5(K/Km)$ (left - right) at 5 hours . . . . .	48
Figure 2.21 $\overline{w'\theta'}$ quadrants at $h_1$ for $w'\theta' = 150$ to $60(W/m^2)$ (top to bottom) and $\gamma = 10$ to $2.5(K/Km)$ (left to right) at 5 hours . . . . .	49
Figure 2.22 $\overline{w'\theta'}$ quadrants at $h_1$ for $w'\theta' = 150$ to $60(W/m^2)$ (top to bottom) and $\gamma = 10$ to $2.5(K/Km)$ (left to right) at 5 hours . . . . .	50
Figure 2.23 Plots of (a) the average downward moving warm air at $h$ $(\overline{w'^-\theta'^+}_h)$ and (b) $\overline{w'^-\theta'^+}_h$ scaled by the average vertical turbulent heat flux $\overline{w'\theta'_s}$ vs time . . . . .	51
Figure 2.24 Plots of (a) the average negative vertical turbulent ve- locity perturbation $w'^-$ at points where the turbulent $\theta'$ perturbation is positive ( $\theta' > 0$ ) (b) $w'^-$ where $\theta' > 0$ . . . . .	51
Figure 2.25 Plots of (a) the average positive potential temperature perturbation $\theta'^+$ at points where the turbulent vertical velocity perturbation is negative ( $w' < 0$ ) (b) $\theta'^+$ where $w' < 0$ . . . . .	52
Figure 2.26 Plots of (a) the average positive potential temperature perturbation $\theta'^+$ at points where the turbulent vertical velocity perturbation is negative ( $w' < 0$ ) (b) $\theta'^+$ where $w' < 0$ . . . . .	52
Figure 2.27 Scaled Entrainment Layer limits ( $\frac{h_1}{h}$ and $\frac{h_0}{h}$ ) vs time . . . . .	54
Figure 2.28 Scaled Entrainment Layer limits ( $z_{f1}$ and $z_{f0}$ ) vs time . . . . .	55
Figure 2.29 Vertical $\frac{\partial \bar{\theta}}{\partial z}$ profiles with threshold at .0002 . . . . .	55

Figure 2.30 Scaled EL depth vs inverse bulk Richardson Number with threshold at .0002	56
Figure 2.31 Vertical $\frac{\partial \bar{\theta}}{\partial z}$ profiles with threshold at .0004	56
Figure 2.32 Scaled EL depth vs inverse Richardson Number with threshold at .0004	57
Figure 2.33 Vertical $\frac{\partial \bar{\theta}}{\partial z}$ profiles with threshold at .0001	57
Figure 2.34 Scaled EL depth vs inverse bulk Richardson Number with threshold at .0001	58
Figure 2.35 Scaled vertical $\frac{\partial \bar{\theta}}{\partial z}$ profiles with threshold at .03	58
Figure 2.36 Plots of scaled EL depth vs $Ri^{-1}$ with CBL height. EL limits and so $\Delta\theta$ based on the $\frac{\partial \bar{\theta}}{\partial z}$ in (a) and the $\frac{\overline{w' \theta'}}{w' \theta'_s}$ profile in (b).	59
Figure 2.37 Scaled EL depth vs $Ri^{-1}$ based on the $\frac{\partial \bar{\theta}}{\partial z}$ profile in log-log coordinates to see likely values of the exponent $b$	59
Figure 2.38 $h$ vs time for all runs	60
Figure 2.39 $\frac{z_f}{h}$ vs Time	61
Figure 2.40 Inverse Richardson number vs time based on the $\frac{\partial \bar{\theta}}{\partial z}$ profile using $\Delta h$ accross the EL in (a) and $\delta\theta$ at $h$ in (b) (2.2)	61
Figure 2.41 Inverse Richardson number vs time based on the $\frac{\overline{w' \theta'}}{w' \theta'_s}$ profile using $\Delta h$ accross the EL in (a) and $\delta\theta$ at $z_f$ in (b) (2.1)	62
Figure 2.42 Scaled entrainment rate vs inverse Richardson number ( $Ri^{-1}$ ), where $Ri$ is based on the $\frac{\partial \bar{\theta}}{\partial z}$ profile using $\Delta h$ accross the EL in (a) and $\delta\theta$ at $h$ in (b) (2.1)	62
Figure 2.43 Scaled entrainment rate vs inverse Richardson number ( $Ri^{-1}$ ), where $Ri$ is based on the $\frac{\overline{w' \theta'}}{w' \theta'_s}$ profile using $\Delta h$ accross the EL in (a) and $\delta\theta$ at $z_f$ in (b) (2.1)	63

# Glossary

**CBL** Convective Boundary Layer

**DNS** Direct Numerical Simulation

**EL** Entrainment Layer

**FA** Free Atmosphere

**FFT** Fast Fourier Transform

**GCM** General Circulation Model

**ML** Mixed Layer

**LES** Large Eddy Simulation

**Ri** Richardson Number, the bulk Richardson Number is  $\frac{gh}{\bar{\theta}_{ML} w^{*2}} \frac{\Delta\theta}{\bar{\theta}(h_1) - \bar{\theta}(h_0)}$ ,  $\Delta\theta =$

**TKE** Turbulence Kinetic Energy

# 1. Introduction

## 1.1 Motivation

The daytime convective atmospheric boundary layer (CBL) over land starts to grow at sunrise when the surface becomes warmer than the air above it. Coherent turbulent structures (thermals) begin to form and rise since their relative warmth causes them to be less dense than their surroundings and so buoyant. The temperature profile of the residual nighttime boundary layer is stable i.e. potential temperature ( $\theta$ , see Section A.1) increases with height. The thermals rise to their neutral buoyancy level overshoot and then overturn or recoil concurrently trapping or enveloping warm stable air from the free atmosphere (FA) above them which is subsequently mixed into the growing turbulent mixed layer (ML) (Stull 1988). This mixing at the top of the CBL is known as entrainment and the region over which it occurs, the entrainment layer (EL). A common, simplified conceptual model of this case is the dry shear free CBL (Sullivan et al. 1998, Federovich et al. 2004 Brooks and Fowler 2012). This model serves as an intellectually accessible way to understand the dynamic and complex CBL and its EL.

CBL height ( $h$ ) and the prediction thereof are important for calculating the concentration of any atmospheric species as well as the sizes of the turbulent structures. In combination with the level at which clouds condense (lifting condensation level) knowledge of EL depth facilitates predictions pertaining to the formation of cumulus clouds. For example cloud cover increases as more thermals rise above their lifting condensation level. Parameterizations

for both CBL growth and EL depth are required in mesoscale and general circulation models (GCMs). Furthermore it is an attractive goal to develop a robust set of scales for this region analogous to Monin-Obukov Theory (Stull 1988, Traumner et al. 2011, Steyn et al. 1999, Nelson et al. 1989, Sorbjan 1996).

Atmospheric CBL entrainment has been studied as a separate phenomenon (Nelson et al. 1989, Sullivan et al. 1998, Federovich et al. 2004, Brooks and Fowler 2012) as well as within the wider topic of entrainment in geophysical flows (Turner 1986). There is broad agreement as to the fundamental scaling parameters and relationships involved. However, the discussion as to how the parameters are defined and measured (Brooks and Fowler 2012, Traumner et al. 2011) and the exact forms of the resulting relationships continues (Sullivan et al. 1998, Federovich et al. 2004 Brooks and Fowler 2012). This prompts me to ask the research questions I build up to in Section 1.2 and outline in Section 1.3.

## 1.2 Relevant Background

### 1.2.1 The Convective Boundary Layer (CBL)

The CBL starts to grow rapidly at sunrise, peaking at midday. Convective turbulence and the dominant upward vertical motions then begin to subside as the surface cools. While the surface is warm, buoyancy driven thermals of uniform potential temperature ( $\theta$ ) and tracer concentration at their cores form and entrain surrounding air laterally as they rise, as well as trapping and mixing in stable warm from above (Stull 1988, Crum et al. 1987). Under conditions of strong convection, buoyantly driven turbulence dominates and shear is insignificant (Fedorovich and Conzemius 2001). Thermal overshoot relative to their neutral buoyancy level, and subsequent entrainment of the warmer air from aloft augments the warming caused by the surface turbulent heat flux ( $\overline{w'\theta'}$ )<sub>s</sub> (see Section A.1) and results in a  $\theta$  jump or inversion at the CBL top (Schmidt and Schumann 1989, Turner 1986). There may

also be a residual inversion from the day before, possibly strengthened by subsidence (Stull 1988, Sullivan et al. 1998).

Lidar images such as Figure 1.1 show the overall structure of the CBL with rising thermals, impinging on the air above (Crum et al. 1987, Traumner et al. 2011).

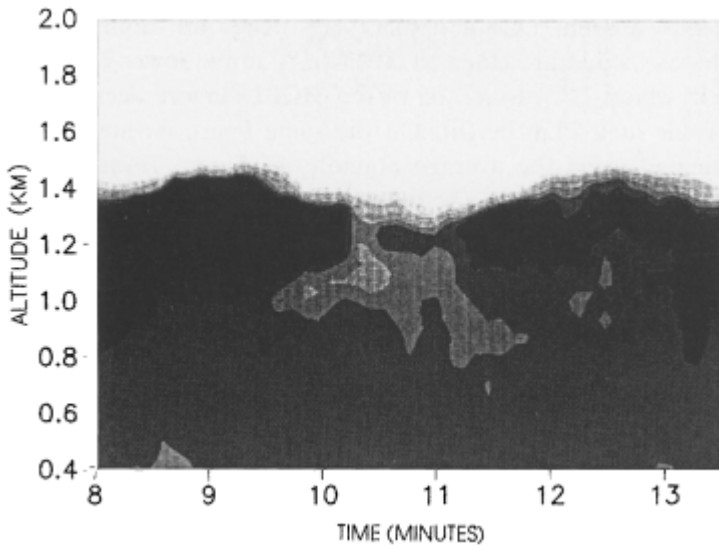


**Figure 1.1:** Lidar backscatter image of the CBL from DuPont et al. 1994. The horizontal distance between the two peaks corresponds to approximately 1700 meters.

This has been effectively modelled using large eddy simulation (LES) by Schmidt and Schumann (1989) who used horizontal slices of turbulent potential temperature and vertical velocity fluctuations ( $\theta'$ ,  $w'$ ) at various vertical levels to show how the thermals form, merge and impinge at the CBL top with concurrent peripheral downward motions. The latter is supported in the LES visualizations of Sullivan et al. (1998). The vertical cross section within the EL in Figure 1.2 shows the relatively cooler thermals and trapped warmer air as well as the closely associated upward motion of cooler air and downward motion of warmer air.

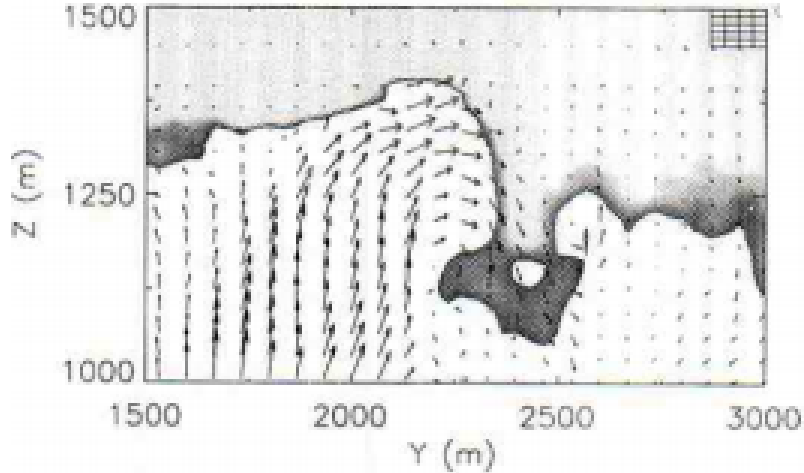


**Figure 1.2:** Flow visualization from Sullivan et al. 1998 showing a modelled CBL thermal enveloping FA air.

On average these convective turbulent structures create a fully turbulent mixed layer (ML) with eddy sizes cascading through an inertial subrange to the molecular scales at which energy is lost via viscous dissipation (Stull 1988). Here, as represented in Figure 1.3,  $\bar{\theta}$  is close to uniform and increases with respect to time due to  $(\overline{w'\theta'})_s$  and the downward flux of entrained stable air at the inversion  $(\overline{w'\theta'})_h$ . ML turbulence is dominated by warm updraughts and cool downdraughts. With proximity to the top the updraughts become relatively cool and warmer FA air from above is drawn downward, so in the ML  $\overline{w'\theta'}$  is positive and decreasing. Directly above the ML the air is stable with intermittent turbulence and, on average, transitions from a uniform ML potential temperature ( $\frac{\partial \bar{\theta}}{\partial z} \approx 0$ ) to a stable lapse rate ( $\gamma$ ). A peak in the average vertical gradient ( $\frac{\partial \theta}{\partial z}$ ) at the inversion represents regions where thermals have exceeded their neutral buoyancy level (see Figure 1.3).

Nelson et al. (1989) outline the stages of CBL growth from when the sub-layers of the nocturnal boundary layer are entrained, until the previous day's capping inversion is reached and a quasi-steady growth is attained. The EL depth relative to CBL height varies throughout these stages and its

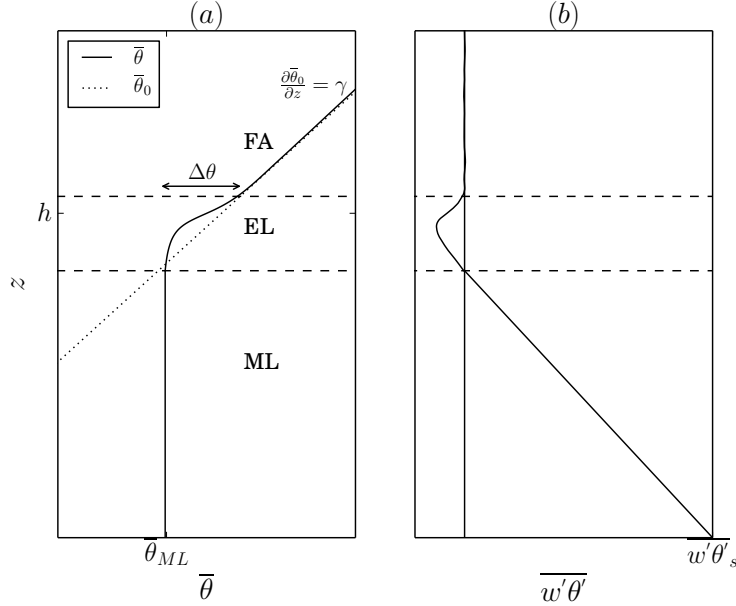


**Figure 1.3:** Idealized vertical average profiles for a dry CBL in the absence of large scale winds or subsidence. (a)  $\bar{\theta}_{ML}$  is the average mixed layer potential temperature.  $h$  is the height of maximum gradient in the  $\bar{\theta}$  profile.  $\bar{\theta}_0$  (dotted line) is the initial  $\bar{\theta}$  profile which has a slope  $\gamma$ . The mixed layer, entrainment layer and free atmosphere are denoted ML, EL and FA respectively. (b)  $w'\theta'$  is the average surface turbulent heat flux. The EL limits (dashed lines) enclose the region of negative  $w'\theta'$ .

relationship to scaled entrainment is hysteretic. Numerical studies typically represent this last quasi-steady phase involving a constant  $(w'\theta')_s$  working against an inversion and or a stable  $\gamma$  (Schmidt and Schumann 1989, Sorbjan 1996, Sullivan et al. 1998, Federovich et al. 2004, Brooks and Fowler 2012, Garcia and Mellado 2014).

### 1.2.2 CBL Height ( $h$ )

The ML is fully turbulent with a uniform average potential temperature ( $\bar{\theta}$ ) which increases sharply over the EL . Aerosol and water vapour concentra-

tions decrease dramatically with transition to the stable upper FA. So any of these characteristics can support a definition of CBL height ( $h$ ). Nelson et al. (1989) defined  $h$  in terms of the percentage of ML air and identified it by eye from Lidar back-scatter images. Traumner et al. (2011) compared four automated methods applied to Lidar images:

- a suitable threshold value above which the air is categorized as ML air,
- the point of minimum (largest negative) vertical gradient,
- the point of minimum vertical gradient based on a fitted idealized curve,
- and the maximum wavelet covariance.

CBL height detection is a wide and varied field. Both Brooks and Fowler (2012) and Traumner et al. 2011 provide more thorough reviews.

Numerical models produce hundreds of local horizontal points from which smooth averaged vertical profiles are obtained, and statistically robust relationships inferred. Brooks and Fowler (2012) applied a wavelet technique to identify the height of maximum covariance in local vertical tracer profiles in their LES study. They compared this method to the gradient method i.e. locating the height of most negative vertical gradient, as well as the height of minimum  $\overline{w'\theta'}$  as shown later in Figure 2.1. This last definition is common among LES and laboratory studies where it has been referred to as the inversion height (Deardorff et al. 1980, Sorbjan 1999, Federovich et al. 2004). Sullivan et al. (1998) clarified that the extrema of the four  $\overline{w'\theta'}$  quadrants (upward warm:  $\overline{w'+\theta'^+}$ , downward warm:  $\overline{w'-\theta'^+}$ , upward cool:  $\overline{w'+\theta'^-}$ , downward cool:  $\overline{w'-\theta'^-}$ ) in the EL more or less correspond to the average point of maximum  $\frac{\partial \theta}{\partial z}$  (see  $h$  in Figure 1.3), whereas the point of minimum  $\overline{w'\theta'}$  was consistently lower. They defined CBL height based on local  $\frac{\partial \theta}{\partial z}$  and applied horizontal averaging as well as two methods based on  $\overline{w'\theta'}$  for comparison.

### 1.2.3 CBL Growth by Entrainment

The CBL grows by trapping pockets of warm stable air between or adjacent to impinging thermal plumes. Traumner et al. (2011) summarize two categories of CBL entrainment:

- Non turbulent fluid can be engulfed between or in the overturning of thermal plumes. This kind of event has been supported by the visualizations in Sullivan et al.'s (1998) LES study as well as in Traumner et al.'s (2011) observations. In both it appeared to occur under a weak inversion or upper lapse rate ( $\gamma$ )
- Impinging thermal plumes distort the inversion interface dragging wisps of warm stable air down at their edges or during recoil under a strong inversion or lapse rate. This type of event is supported by the findings of both Sullivan et al. (1998) and Traumner et al. (2011).

Shear induced instabilities do occur at the top of the atmospheric boundary layer and in some laboratory studies of turbulent boundary layers, under conditions of very high stability, breaking of internal waves have been observed. Entrainment via the former is relatively insignificant in strong convection, and the latter has not been directly observed in real or modeled atmospheric CBLs over the range of conditions considered here (Traumner et al. 2011, Sullivan et al. 1998).

### 1.2.4 The CBL Entrainment Layer (EL)

The ML is fully turbulent but the top is characterized by stable air with intermittent turbulence due to the higher reaching thermals. Garcia and Mellado (2014) demonstrate that the EL is subdivided in terms of length and buoyancy scales. That is, the lower region is comprised of mostly turbulent air with pockets of stable warmer air that are quickly mixed, and so scales with the convective scales (see section 1.2.6). Whereas the upper region is mostly stable apart from the impinging thermals so scaling here is more influenced by the lapse rate ( $\gamma$ ). In the EL the average vertical heat

flux,  $\overline{w'\theta'}$ , switches sign relative to that in the ML. The fast updraughts are now relatively cool  $\overline{w'+\theta'-}$ . In their analysis of the four  $\overline{w'\theta'}$  quadrants Sullivan et al. (1998) concluded that the overall net dynamic in this region is downward motion of warm air ( $\overline{w'-\theta'+}$ ) from the free atmosphere (FA) since the other three quadrants effectively cancel.

In terms of tracer concentration, and for example based on a Lidar backscatter profile, there are two ways to conceptually define the EL. It can be thought of as the range in space (or time) over which local CBL height varies (Crum et al. 1987) or a local region over which the concentration (or back-scatter intensity) transitions from ML to FA values (Traumner et al. 2011). The latter can be estimated using either curve-fitting or wavelet techniques (Traumner et al. 2011, Steyn et al. 1999, Brooks and Fowler 2012).

Brooks and Fowler apply a wavelet technique to tracer profiles for the determination of EL limits, in their 2012 LES study. However, it is more common in numerical modelling and laboratory studies for the EL limits to be defined based on the average vertical turbulent heat flux ( $\overline{w'\theta'}$ ) i.e. the points enclosing the negative region as shown in Figure 1.3 (Deardorff et al. 1980, Federovich et al. 2004, Garcia and Mellado 2014). Bulk models based on the representation in Figure 1.3 assume the region of negative  $\overline{w'\theta'}$  coincides with the region where  $\bar{\theta}$  transitions from the ML value to the FA value (Deardorff 1979, Federovich et al. 2004) but no modelling studies use the vertical  $\bar{\theta}$  profile to define the EL.

Since  $\bar{\theta}$  modeled by an LES is not strictly constant with respect to height in the ML (Federovich et al. 2004), a threshold value for  $\bar{\theta}$  or its vertical gradient must be chosen to identify the lower EL limit. In their 2012 LES study Brooks and Fowler encountered inconsistencies when determining the EL limits from the average tracer profile. Although their tracer profile was quite different to a simulated CBL  $\bar{\theta}$  profile, this could serve as cautionary note.

Our understanding of the characteristics and dynamics of the atmospheric CBL entrainment layer evolves with the increasing body of measurement (Traumner et al. 2011, Nelson et al. 1989), laboratory (Deardorff et al. 1980) and numerical studies (Deardorff 1972, Sorbjan 1996, Sullivan et al. 1998, Federovich et al. 2004, Brooks and Fowler 2012, Garcia and Mellado 2014). Parameterizations for CBL growth and EL depth are derived based on bulk models and are evaluated using LES output and measurements (Federovich et al. 2004, Boers 1989). So the relationship between theory, numerical simulation and measurement is inextricable and any study based on one must refer to at least one of the others.

### 1.2.5 Modelling the CBL and EL

#### Bulk Models

Bulk models for the Convective Boundary layer (CBL) based on average, vertical profiles of ML quantities can be subdivided into: (i) zero order as represented in Figure 1.4 and (ii) first (and higher) order bulk models as represented in Figure 1.3. Order refers to the number of prognostic variables, and increased order corresponds to increasing complexity in the shape of the  $\bar{\theta}$  and  $\overline{w'\theta'}$  profiles at the top of the ML.

Zero order bulk models assume an ML of uniform potential temperature ( $\bar{\theta}_{ML}$ ) topped by an infinitesimally thin layer across which there is a temperature jump ( $\delta\theta$ ) and above which is a constant lapse rate ( $\gamma$ ). The assumed average vertical turbulent heat flux,  $\overline{w'\theta'}$ , decreases linearly from the surface up, reaching a maximum negative value  $(\overline{w'\theta'})_h$ . This is a constant proportion of the surface value, usually  $-2(\overline{w'\theta'})_s$  (see Section 4 in Tennekes 1973 for a discussion). At the temperature inversion  $\overline{w'\theta'}$  jumps to zero across the infinitesimally thin layer. Equations for the evolution of CBL height,  $\bar{\theta}_{ML}$  and  $\delta\theta$  are derived on this basis (Tennekes 1973).

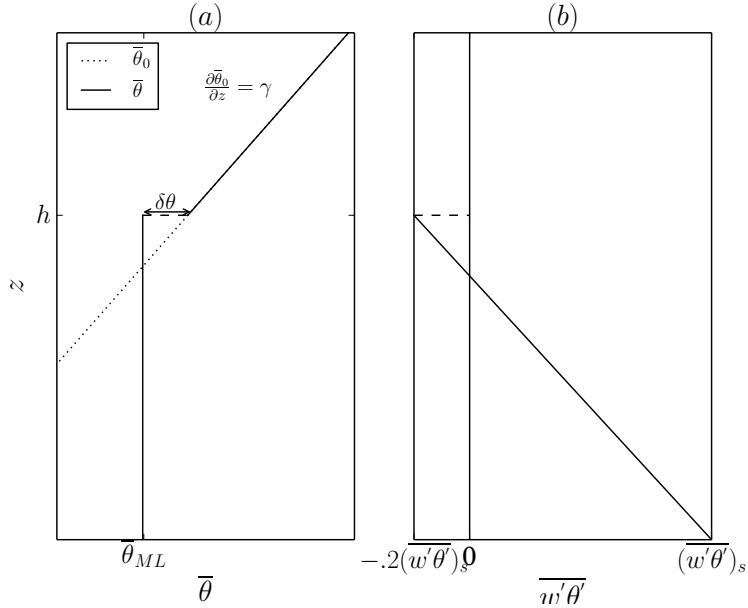


**Figure 1.4:** Simplified version of Figure 1.3 such that the EL is infinitesimally thin. (a)  $h$  is the height of the inversion and  $\delta\theta$  the corresponding temperature jump, that is, the difference between  $\bar{\theta}_{ML}$  and  $\bar{\theta}_0(h)$ . This is different, although related, to the jump across the EL in Figure 1.3  $\Delta\theta$ . (b) The  $w'\theta'$  profile is linear and decreasing until it reaches a maximum negative value at  $h$  of  $-.2(\overline{w'\theta'})_s$ . Here there is a discontinuity as it jumps to zero.

If the CBL height ( $h$ ) is rising, air is being drawn in from the stable free atmosphere (FA) layer above and cooled i.e. it is decreasing in enthalpy. The rate of decrease in enthalpy with respect to time is  $c_p\rho\delta\theta\frac{dh}{dt}$  (see Section A.1) per unit of horizontal area where  $\frac{dh}{dt}$  is the entrainment rate ( $w_e$ ). Since the lapse rate above the inversion is stable Tennekes (1973) equates this enthalpy loss to the average vertical turbulent heat flux at the inversion

$$\delta\theta\frac{dh}{dt} = -(\overline{w'\theta'})_h. \quad (1.1)$$

The ML warming rate is arrived at via the simplified Reynolds averaged

conservation of enthalpy, for which the full derivation is shown in Section A.3.

$$\frac{\partial \bar{\theta}_{ML}}{\partial t} = -\frac{\partial}{\partial z} \overline{w' \theta'}. \quad (1.2)$$

Assuming  $\overline{w' \theta'}$  has a constant slope this becomes

$$\frac{\partial \bar{\theta}_{ML}}{\partial t} = \frac{(\overline{w' \theta'})_s - (\overline{w' \theta'})_h}{h} \quad (1.3)$$

and the evolution of the temperature jump ( $\delta\theta$ ) depends on the rate of CBL height ( $h$ ) increase, the upper lapse rate  $\gamma$  and the ML warming rate

$$\frac{d\delta\theta}{dt} = \gamma \frac{dh}{dt} - \frac{d\bar{\theta}_{ML}}{dt}. \quad (1.4)$$

An assumption about the vertical heat flux at the inversion ( $h$ ), such as the entrainment ratio, closes this set

$$\frac{(\overline{w' \theta'})_h}{(\overline{w' \theta'})_s} = -.2. \quad (1.5)$$

The relevant quantities in equations 2.2 through 2.5 are idealized, ensemble averages. There is some variation within this class of model. For example the rate equation for  $h$  (entrainment relation) can alternatively be derived based on the turbulent kinetic energy budget (Federovich et al. 2004) but they are all based on the simplified  $\bar{\theta}$  and  $\overline{w' \theta'}$  profiles outlined above.

First (and higher) order models assume an EL of finite depth at the top of the ML, defined by two heights: the top of the ML ( $h_0$ ) and the point where FA characteristics are resumed ( $h_1$ ). The derivations are more complex and involve assumptions about the EL i.e.:

- $\Delta h = h_1 - h_0 = \text{Constant}$  (Betts 1974)
- $\Delta h = h_1 - h_0$  is related to the zero-order jump at  $h$  by two right angled

triangles with opposite sides of lengths  $h_1 - h$  and  $h - h_0$  (Batchvarova and Gryning 1994)

- $\Delta h$  or maximum overshoot distance  $d \propto \frac{w^*}{N}$  where  $w^*$  is the convective vertical velocity scale and  $N = \sqrt{\frac{g}{\theta} \frac{\partial \theta}{\partial z}}$  is the Brunt-Vaisala frequency (Stull 1973)
- For  $h_0 < z < h_1$   $\bar{\theta} = \bar{\theta}_{ML} + f(z, t)\Delta\theta$  where  $f(z, t)$  is a dimensionless shape factor (Deardorff 1979, Federovich et al. 2004)

Although development of these models is beyond the scope of this thesis, they are mentioned to give context to the parameterizations considered in Sections 1.2.6 and 1.2.6.

### Numerical Simulations

Numerical simulation of the CBL is carried out by solving the Navier Stokes equations, simplified according to a suitable approximation, on a discrete grid. Types of simulations can be grouped according to the scales of motion they resolve. In direct numerical simulations (DNS) the full range of spatial and temporal turbulence are resolved from the size of the domain down to the smallest dissipative scales i.e. the Kolmogorov micro-scales (Kolmogorov 1962). This requires a dense numerical grid and so can be computationally prohibitive.

In an LES motion on scales smaller than the grid spacing are filtered out and parameterized by a sub-grid scale closure model. General circulation models (GCM) solve the Navier Stokes equations on a spherical grid and parameterize smaller scale processes including convection and cloud cover. LES has increasingly been used to better understand the CBL since Dear-dorff (1972) applied this relatively new method for this purpose. Sullivan et al. (1998), Federovich et al. (2004) and Brooks and Fowler in (2012) used it to study the structure and scaling behaviour of the EL.

### 1.2.6 Scales and Scaling Relations of the CBL and EL

#### Length Scale ( $h$ )

Deardorff (1972) demonstrated that dominant turbulent structures in penetrative convection scale with CBL height, which he referred to as the inversion height but measured as the height of minimum average vertical heat flux:  $z_f$  as shown later in Figure 2.1 (Deardorff et al. 1980). Since then, the distinction between the two has been clarified (see Section 1.2.2) and here  $h$  refers strictly to the height of maximum average potential temperature gradient. There are alternatives. For example turbulence based definitions, such as the velocity variance and the distance over which velocity is correlated with itself, represent the current turbulent dynamics rather than the recent turbulence history as does  $h$  (Traumner et al. 2011).

#### Convective Velocity Scale ( $w^*$ )

Given an average surface vertical heat flux  $(\overline{w'\theta'})_s$  a surface buoyancy flux can be defined as  $\frac{g}{\theta}(\overline{w'\theta'})_s$  which gives the convective velocity scale when multiplied by the appropriate length scale. Since the result has units  $\frac{m^3}{s^3}$  a cube root is applied

$$w^* = \left( \frac{gh}{\overline{\theta}} (\overline{w'\theta'})_s \right)^{\frac{1}{3}}. \quad (1.6)$$

Deardorff (1970) confirmed that this effectively scaled the local vertical turbulent velocity perturbations ( $w'$ ) in the CBL. Sorbjan's (1996) work supports this, even at the CBL top. The CBL entrainment rate ( $w_e = \frac{dh}{dt}$ ) depends on the magnitude of  $w'$  which is driven by  $\overline{w'\theta'}_s$ . Stability aloft suppresses  $\frac{dh}{dt}$  so influence of  $\gamma$  is indirectly accounted for via  $h$  in  $w^*$ .

### Convective Time Scale ( $\tau$ )

It follows that the time a thermal, travelling at velocity scaled by  $w^*$ , takes to reach the top of the CBL i.e. travel a distance  $h$  is scaled by

$$\tau = \frac{h}{\left(\frac{gh}{\theta} \overline{w' \theta'}\right)^{\frac{1}{3}}}. \quad (1.7)$$

This is also referred to as the convective overturn time scale. Sullivan et al. (1998) showed a linear relationship between  $h$  and time scaled by  $\tau$ . An alternative is the Brunt-Vaisala frequency i.e. the time scale associated with the buoyant thermals overshooting and sinking (Federovich et al. 2004). The ratio of these two time-scales forms a parameter which characterizes this system (see Sorbjan 1996 and Deardorff 1979).

### Temperature Scale ( $\theta^*$ )

The CBL temperature fluctuations  $\theta'$  are influenced by  $\overline{w' \theta'}$  from both the surface and the CBL top. Deardorff (1970) showed that an effective scale based on the convective velocity scale is

$$\theta^* = \frac{(\overline{w' \theta'})_s}{w^*}. \quad (1.8)$$

Whereas Sorbjan (1996) showed that with proximity to the CBL top the effects of FA stability  $\gamma$  become more important.

### Buoyancy Richardson Number (Ri)

The flux Richardson ( $R_f$ ) number expresses the balance between mechanical and buoyant production of turbulent kinetic energy (TKE) and is obtained from the ratio of these two terms in the TKE budget equation (See Appendix, Stull 1988):

$$R_f = \frac{\frac{g}{\theta} \left( \overline{w' \theta'} \right)}{\overline{u'_i u'_j} \frac{\partial \bar{U}_i}{\partial x_j}}. \quad (1.9)$$

Assuming horizontal homogeneity and vertically constant subsidence yields

$$R_f = \frac{\frac{g}{\theta} \left( \overline{w' \theta'} \right)}{\overline{u' w'} \frac{\partial \bar{U}}{\partial z} + \overline{v' w'} \frac{\partial \bar{V}}{\partial z}}. \quad (1.10)$$

Applying first order closure to the flux terms, i.e. assuming they are proportional to the vertical gradients, gives the gradient Richardson number ( $R_g$ )

$$R_g = \frac{\frac{g}{\theta} \frac{\partial \bar{\theta}}{\partial z}}{\left( \frac{\partial \bar{U}}{\partial z} \right)^2 + \left( \frac{\partial \bar{V}}{\partial z} \right)^2}, \quad (1.11)$$

However, in the EL buoyancy acts to suppress buoyant production of TKE. Applying a bulk approximation to the denominator, and expressing it in terms of scales yields a squared ratio of two time scales

$$R_g = \frac{\frac{g}{\theta} \frac{\partial \bar{\theta}}{\partial z}}{\frac{U^{*2}}{L^2}} = N^2 \frac{L^2}{U^{*2}}, \quad (1.12)$$

where  $U^*$  and  $L^*$  are appropriate velocity and length scales. Applying the bulk approximation to both the numerator and denominator yields the bulk Richardson number:

$$R_b = \frac{\frac{g}{\theta} \Delta \theta L^*}{U^{*2}}. \quad (1.13)$$

A natural choice of length and velocity scales for the CBL are  $h$  and  $w^*$  giving the convective or buoyancy Richardson number:

$$Ri = \frac{\frac{g}{\theta} \Delta \theta h}{w^{*2}}. \quad (1.14)$$

Where  $\Delta \theta$  can be replaced by  $\delta \theta$  as in Federovich et al. (2004) and Garcia and Mellado (2014). Ri can also be arrived at by considering the principal forcings of the system, or from non-dimensionalizing the entrainment relation derived analytically (Tennekes 1973, Deardorff 1972). It is central to any study on CBL entrainment (Sullivan et al. 1998, Federovich et al. 2004,

Traumner et al. 2011, Brooks and Fowler 2012).

### Relationship of Entrainment Rate to Richardson Number

The relationship between scaled entrainment rate and the buoyancy Richardson number ( $Ri$ )

$$\frac{w_e}{w^*} \propto Ri^a \quad (1.15)$$

is arrived at according to the zero order bulk model through thermodynamic arguments, or by integration of the conservation of enthalpy or turbulent kinetic energy equations over the growing CBL. (Tennekes 1973, Deardorff 1979, Federovich et al. 2004). It has been verified in numerous laboratory and numerical studies (Deardorff et al. 1980, Sullivan et al. 1998, Federovich et al. 2004, Brooks and Fowler 2012), but there is still some unresolved discussion as to the exact value of  $a$ . It seems there are two possible values,  $-\frac{3}{2}$  and  $-1$ , the first of which Turner (1986) suggested occurs at high stability when buoyant recoil of impinging thermals becomes more important than their convective overturning. Assume that an impinging thermal supplies kinetic energy ( $K$ ) per unit time and per unit area for entrainment, in terms of appropriate length and time scales  $L^*$  and  $t^*$  as follows

$$K \propto \frac{\bar{\rho} L^{*3} U^{*2}}{L^{*2} t^*}, \quad (1.16)$$

and that the corresponding change in potential energy per unit time and area of the rising CBL is

$$\Delta P \propto g \Delta \theta h \frac{dh}{dt}. \quad (1.17)$$

If  $L^*$  is the penetration depth of the thermals travelling at velocity scaled by  $w^*$  against a decelerating force  $g \frac{\Delta \rho}{\bar{\rho}}$

$$L^* = \frac{w^{*2} \bar{\theta}}{\Delta \theta}. \quad (1.18)$$

and  $t^*$  is the response time of the inversion layer to a thermal of length  $h$

$$t^* = \sqrt{h \frac{\bar{\theta}}{g\Delta\theta}} \quad (1.19)$$

then assuming all of  $K$  is transferred to the change in potential energy ( $\Delta P$ ) and using the CBL velocity, yields

$$\frac{\frac{dh}{dt}}{w^*} \propto \frac{w^{*2}\bar{\theta}}{g\Delta\theta h} \sqrt{\frac{\bar{\theta}w^{*2}}{g\Delta\theta h}}, \quad (1.20)$$

i.e.

$$\frac{w_e}{w^*} \propto Ri^{-\frac{3}{2}}. \quad (1.21)$$

Adding further complexity to this discussion, Federovich et al. (2004) suggest that this power law relationship ( $a = -\frac{3}{2}$ ) can be arrived at through defining the  $\theta$  jump across the EL (see Figure 1.3).

### Relationship of Entrainment Layer Depth to Richardson Number

A relationship of the scaled entrainment layer EL depth to  $Ri$

$$\frac{\Delta h}{h} \propto Ri^b \quad (1.22)$$

is arrived at by considering the deceleration of a thermal as it overshoots its neutral buoyancy level (Nelson et al. 1989). If the velocity of the thermal is assumed to be proportional to  $w^*$  and the decelerating force is due to the buoyancy difference, or  $\theta$  jump, then the distance the thermal overshoots ( $d$ ) can be approximated by

$$d \propto \frac{w^{*2}}{\frac{g}{\bar{\theta}_{ML}}\Delta\theta}. \quad (1.23)$$

If the EL depth is proportional to the overshoot distance ( $d$ ) then

$$\frac{\Delta h}{h} \propto \frac{w^{*2}}{\frac{g}{\bar{\theta}_{ML}}h\Delta\theta} = Ri^{-1}. \quad (1.24)$$

Alternatively, Boers 1989 integrated the internal ( $U$ ), potential ( $P$ ) and kinetic ( $K$ ) energy over a hydrostatic atmosphere

$$U = \frac{c_v}{g} \int_0^{p_0} T dp. \quad (1.25)$$

$$P = \frac{R}{c_v} U, \quad (1.26)$$

and

$$K = \frac{1}{2} \int_0^{p_0} \frac{w^2}{g} dp. \quad (1.27)$$

$p_0$  is the surface pressure,  $R$  and  $c_v$  are the gas constant and heat capacity of dry air at constant volume.  $T$  is temperature. Initially there is a flat infinitesimally thin inversion interface which is distorted by an impinging thermal. The resulting height difference is assumed sinusoidal and an average  $\Delta h$  is obtained by integrating over a wavelength. At this point, no entrainment is assumed to have occurred and all of the initial kinetic energy ( $K_i$ ) has been transferred to the change in potential energy ( $\Delta P$ ).

$$K_i = P_f - P_i = \Delta P \quad (1.28)$$

Assuming a dry adiabatic atmosphere and that the vertical velocity in the layer below the inversion can be approximated by the convective velocity scale ( $w^*$ ), the following expression is reached

$$\left( \frac{\Delta h}{h} \right)^2 \propto \frac{T_0 w^{*2}}{g \Delta \theta h}. \quad (1.29)$$

The reference temperature,  $T_0$ , can be replaced by  $\bar{\theta}_{ML}$  to give

$$\frac{\Delta h}{h} \propto Ri^{-\frac{1}{2}} \quad (1.30)$$

### 1.3 Research Questions

A simplified conceptual model of the dry, shear-free CBL in the absence of large scale winds is represented in Figure 1.3. The two principal external parameters in this case, are the average vertical turbulent surface heat flux ( $\overline{w'\theta'}$ )<sub>s</sub> and the upper lapse rate ( $\gamma$ ) (Federovich et al. 2004, Sorbjan 1996). They have opposing effects, that is  $\overline{w'\theta'}$ <sub>s</sub> drives upward turbulent velocity ( $w'^+$ ) and so CBL growth ( $w_e$ ) whereas  $\gamma$  suppresses it. Conversely they both cause positive turbulent potential temperature perturbations ( $\theta'^+$ ) and so warming of the CBL. In the EL the thermals from the surface are now relatively cool. They turn downwards as they interact with the stable FA concurrently bringing down warmer air. Sullivan et al. (1998) demonstrated these dynamics by partitioning  $w'\theta'$  into four quadrants. Sorbjan (1996) asserted and showed that in this region the turbulent potential temperature perturbations ( $\theta'$ ) are strongly influenced by  $\gamma$  whereas the turbulent vertical velocity perturbations ( $w'$ ) are almost independent thereof. Inspired by these two studies and to gain some insight into the dynamics of this idealized CBL I ask **Q1: How do the distributions of local CBL height, and the joint distributions of  $w'$  and  $\theta'$  within the EL, vary with  $(\overline{w'\theta'})_s$  and  $\gamma$ ?**

The relationship between scaled EL depth and  $Ri$

$$\frac{\Delta h}{h} \propto Ri^b \quad (1.15)$$

has been explored and justified in field measurement, laboratory and numerical studies. There is disagreement with respect to its exact form, in part stemming from variation in height and  $\theta$  jump definitions, but in general its magnitude relative to  $h$  decreases with increasing  $Ri$ . Although referred to in most relevant studies and relied upon in analytical models, the vertical average potential temperature profile has not been used to define the EL (Deardorff et al. 1980, Nelson et al. 1989, Federovich et al. 2004, Boers 1989, Brooks and Fowler 2012). This leads me to ask **Q2: Can the EL limits be defined based on the  $\bar{\theta}$  profile and what is the relationship of**

**the resulting depth ( $\Delta h$ ) to  $Ri$ ?**

A further simplification to the dry, shear-free, CBL model without large scale velocities, is to regard the EL depth as infinitesimally small as in Figure 1.4. The relationship of the scaled, time rate of change of  $h$  (entrainment rate:  $w_e$ ) to  $Ri$  can be derived based on this model (Tennekes 1973, Deardorff 1979, Federovich et al. 2004)

$$\frac{w_e}{w^*} \propto Ri^a. \quad (1.22)$$

This will be referred to as the entrainment relation. Although that there is such a relationship is well established, discussion as to the power exponent of  $Ri$  is unresolved and results from studies justify values of both  $-\frac{3}{2}$  and  $-1$ . See Traumner et al. (2011) for a summary and review. Turner (1986) explains this disparity in terms of entrainment mechanism such that the higher value occurs when thermals recoil rather than overturn in response to a stronger  $\theta$  jump (or inversion). Whereas Sullivan et al. (1998) notice a deviation from the lower power ( $-1$ ) at lower  $Ri$  and attribute it to the effect of the shape of  $\bar{\theta}$  within a thicker EL. Both Federovich et al. (2004) and Garcia and Mellado (2014) show how the definition of the  $\theta$  jump influences the time rate of change of  $Ri$  and so effects  $a$ . **Q3: How does defining the  $\theta$  jump based on the vertical  $\bar{\theta}$  profile across the EL as in Figure 1.3 vs at the inversion ( $h$ ) as in Figure 1.4, affect the entrainment relation and in particular  $a$ ?**

## 1.4 Approach to Research Questions

### General Setup

I modelled the dry shear free CBL and EL using LES, specifically the cloud resolving model System for Atmospheric Modelling (SAM) to be outlined in Chapter 3. An ensemble of 10 cases was run to obtain true ensemble averages and turbulent potential temperature variances ( $\theta'$ ), each case had a

domain of area  $3.2 \times 4.8 \text{ Km}^2$ . Grid spacing was influenced by the resolution study of Sullivan and Patton (2011) and the vertical grid within the EL was of higher resolution than that applied in other comparable work. The runs were initialized with a constant  $\overline{w'\theta'}_s$  acting against a uniform  $\gamma$ . So, the  $\theta$  jump arose from the overshoot of the thermals, rather than being initially imposed as in Sullivan et al. (1998) and Brooks and Fowler (2012).

## Verifying Output

Before addressing the questions stated in Section 1.3 I will examine the modeled output to make sure it represents a realistic turbulent CBL in Chapter 3 section 2. I will verify that the averaged vertical profiles are as expected and coherent thermals are being produced. FFT energy density spectra will show if there is adequate scale separation between the structures of greatest energy and the grid spacing, and that realistic, isotropic turbulence is being modelled.

### Q1

The EL can be thought of in terms of the distribution of individual thermal heights, or local heights. Sullivan et al. (1998) measured local height by locating the vertical point of maximum  $\theta$  gradient, and observed the effects of varying  $Ri$  on the resulting distributions. However this method is problematic when gradients in the upper profile exceed that at the inversion (Brooks and Fowler 2012). Steyn et al. (1999) fitted an idealized curve to a lidar backscatter profile. This method produces a smooth curve based on the full original profile on which a maximum can easily be located. I will apply a multi-linear regression method outlined in Vieth (2011) to the local  $\theta$  profile, representing the ML, EL and FA each with a separate line segment. From this fit, I will locate the ML top ( $h_0^l$ ). I'll observe how the resulting distributions are effected by changes in  $(w'\theta')_s$  and  $\gamma$  using histograms and verify that the 2d horizontal  $h_0^l$  surface corresponds to the location of the thermals in the EL, in Chapter 3 Section 3.

Sullivan et al. (1998) broke the turbulent vertical heat flux  $w'\theta'$  into four quadrants and used this combined with local flow visualizations to show how CBL thermals impinge and draw down warm air from above. Mahrt and Paumier (1984) used 2 dimensional contour plots of local  $w'$  and  $\theta'$  measurements to analyze their joint distributions. In his 1996 LES study Sorbjan showed that in the EL,  $\theta'$  is strongly influenced by  $\gamma$  whereas  $w'$  is independent thereof. Influenced by these three studies, I will use 2 dimensional histograms at three levels within the EL to look at how the distributions of local  $w'$  and  $\theta'$  are effected by changes in  $\gamma$  and  $(\overline{w'\theta'})_s$ . I will magnify the effects of  $\gamma$ , by applying the convective scales,  $\theta^*$  and  $w^*$  in Chapter 3 Section 4.

## Q2

Here I define the CBL height as the location of maximum vertical  $\bar{\theta}$  gradient as in Figure 2.1. The lower and upper EL limits are then the points at which  $\frac{\partial \bar{\theta}}{\partial z}$  significantly exceeds zero and where it resumes  $\gamma$ . The lower limit requires choice of a threshold value which should be small, positive and less than  $\gamma$ . Since it is somewhat arbitrary I will compare results based on three different threshold values in Chapter 3 section 5. Federovich et al. (2004) and Brooks and Fowler (2012) defined the EL in terms of the vertical  $\overline{w'\theta'}$  profiles as in Figure 2.1 but disagreed on the shape of the relationship of scaled EL depth to Ri (equation 2.1). As well as observing this relationship using the height definitions based on the  $\bar{\theta}$  profile, I will apply the definitions based on the  $\overline{w'\theta'}$  profile for comparison with the Brooks and Fowler (2012) and Federovich et al. (2004) in Chapter 3 section 4.

## Q3

As discussed in see Section 1.2.6 the form of the entrainment relation is thought to vary based on the mechanism that initiate entrainment, which

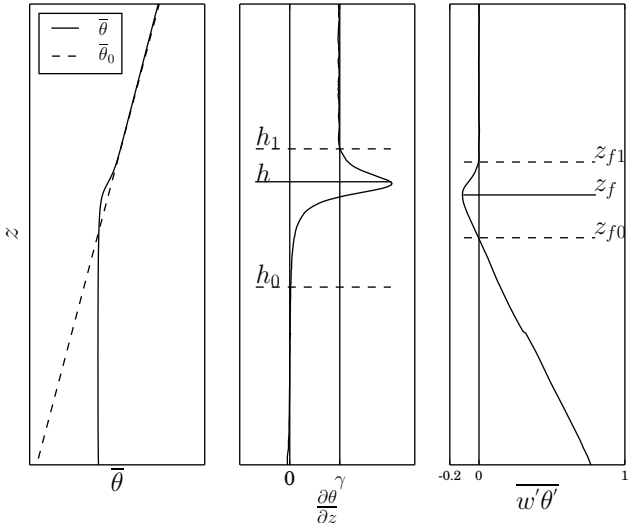


**Figure 1.5:** Height definitions based on the average vertical profiles.  $\theta_0$  is the initial potential temperature.

CBL Height	ML $\bar{\theta}$	$\theta$ Jump	Ri
$h$	$\bar{\theta}_{ML} = \frac{1}{h} \int_0^h \bar{\theta}(z) dz$	$\delta\theta = \bar{\theta}(h_1) - \bar{\theta}(h_0)$	$Ri_\Delta = \frac{\frac{g}{\bar{\theta}_{ML}} \delta\theta h}{w^{*2}}$
		$\Delta\theta = \bar{\theta}_0(h) - \bar{\theta}_{ML}$	$Ri_\delta = \frac{\frac{g}{\bar{\theta}_{ML}} \Delta\theta h}{w^{*2}}$

**Table 1.1:** Definitions based on the vertical  $\bar{\theta}$  profile in Figure 2.1. To obtain those based on the  $w' \theta'$  profile, replace  $h_0$ ,  $h$  and  $h_0$  with  $z_{f0}$ ,  $z_f$  and  $z_{f1}$

in turn depends on the magnitude of Ri. Furthermore the ways in which the height and  $\theta$  jump are defined have an effect. I will vary the definition of the  $\theta$  jump as outlined in table 2.2 in order to discern between how this, and variation in initial conditions, influence the entrainment relation and in particular  $a$ . I will reproduce this analysis using height definitions based on  $w' \theta'$  for comparison with the results of Federovich et al. (2004).

## 2. Results

### 2.1 Description of Runs

All 10 member cases of the ensemble were carried out on a 3.2 x 4.8 Km horizontal domain ( $\Delta x = \Delta y = 25m$ ,  $nx = 128$ ,  $ny = 192$ ).  $nx$ ,  $ny$  were chosen based on the optimal distribution across processor nodes. The vertical grid ( $nz = 312$ ) was of higher resolution around the entrainment layer (EL) ( $\Delta z = 5m$ ), and lower below and above it ( $\Delta z = 10$  to  $100m$ ). Grid size was chosen so that a full spectrum of turbulence would be resolved within the EL in line with the findings of Sullivan and Patton in [24]. The 7 runs vary depending on surface heat flux ( $\overline{w'\theta'_s}$ ) and initial lapse rate ( $\gamma$ ).

$\overline{w'\theta'_s} / \gamma$	10 (K/Km)	5 (K/Km)	2.5 (K/Km)
150 (W/m <sup>2</sup> )	✓	✓ <sup>1</sup>	
100 (W/m <sup>2</sup> )	✓	✓	
60 (W/m <sup>2</sup> )	✓	✓	✓

**Table 2.1:** Runs in terms of  $\overline{w'\theta'_s}$  and initial lapse rate  $\gamma$

---

<sup>1</sup>Incomplete run: EL exceeded high resolution vertical grid after 7 hours

## 2.2 Relevant Definitions

Here, the CBL height and EL limits are defined based on the vertical  $\frac{\partial \bar{\theta}}{\partial z}$  profile. Namely, the CBL height  $h$  is the point where  $\frac{\partial \bar{\theta}}{\partial z}$  is maximum, the lower EL limit is the point at which  $\frac{\partial \bar{\theta}}{\partial z}$  first increases significantly from zero, i.e. exceeds a threshold value, above the surface layer, and the upper EL limit  $h_1$  is the point where  $\frac{\partial \bar{\theta}}{\partial z}$  resumes  $\gamma$ . (Figure 2.1)

As Brooks and Fowler point out in [4], when using an average vertical tracer profile there is no universal criteron for a significant gradient. So a threshold value for the lower EL limit ( $h_0$ ) was chosen such that it was positive, small i.e. an order of magnitude less than  $\gamma$  and the same for all runs. For the sake of rigor, the main corresponding result was calculated based on two additional threshold values in Section 2.6.1.

The temperature jump is defined here as the difference in  $\bar{\theta}$  accross the EL. So, it is larger than those used by Federovich et al. in [11] to verify their zero order model and Sullivan et al. in [23] (Table 2.2). We also define a zero-order type temperature jump as the difference between the mixed layer (ML) average potential temperature ( $\bar{\theta}$ ) less ( $\bar{\theta}$ ) at  $h$  on the initial profile.

CBL Height	$\theta$ Jump	Richardson Number
$h$	$\Delta\theta = \bar{\theta}(h_1) - \bar{\theta}(h_0)$	$Ri = \frac{\frac{g}{\theta} \delta\theta h}{w^{*2}}$
	$\delta\theta = \bar{\theta}_{ML} - \bar{\theta}_0(h)$	$Ri_\delta = \frac{\frac{g}{\theta} \Delta\theta h}{w^{*2}}$

**Table 2.2:** Relevant Definitions used in this Study

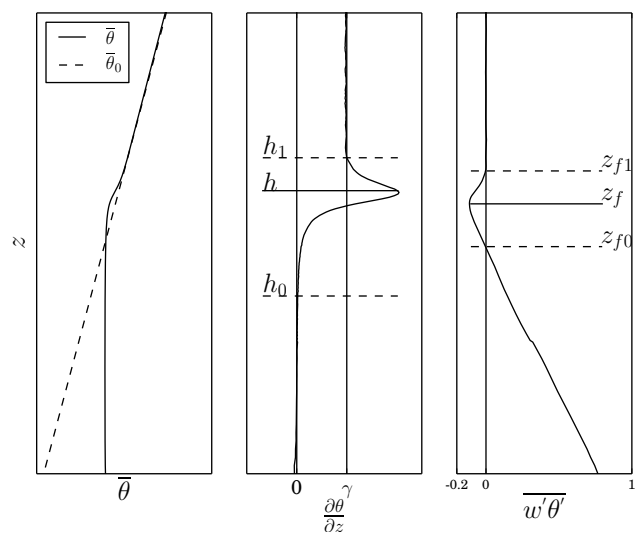


**Figure 2.1:** CBL height and EL limit definitions based on the  $\frac{\partial \bar{\theta}}{\partial z}$  and  $\overline{w' \theta'}$  profiles.

## 2.3 Verifying the Model Output

### 2.3.1 Time till well-mixed

Time must be allowed to establish statistically steady turbulent flow. Sullivan et al. in [23] recommended 10 eddie turnover times based on the convective time scale  $\tau = \frac{h}{w^*} = \frac{h}{\left(\frac{gh}{\bar{\theta}_{ML}}(w'\theta'_s)\right)^{\frac{1}{3}}}$ , and Brooks and Fowler in [4] chose a simulated time of 2 hours. For all of the runs, at least 10 eddie turnover times were completed by 2 simulated hours (Figure 2.2). Although each run has a distinct convective velocity scale that increases with time ( $w^*(time)$ ), dividing boundary layer height ( $h$ ) by it to obtain  $\tau$  results in a collapse from 7 to 3 curves, one for each  $\gamma$ .

A measureable well mixed layer (ML) and EL based on the horizontally averaged, ensemble averaged potential temperature ( $\bar{\theta}$ ) profile develops after 2 hours (Figure ??). After 2 or 3 hours the EL is fully contained within the vertical region of high resolution.

Averaged heat fluxes ( $\overline{w'\theta'}$ ) (Figure 2.4) and root mean squared vertical velocity perturbations ( $\sqrt{w'^2}$ ) (Figure ??) become self similar and are scaled well by the surface heat flux ( $\overline{w'\theta'_s}$ ) and the convective velocity scale ( $w^*$ ) respectively after 2 hours.

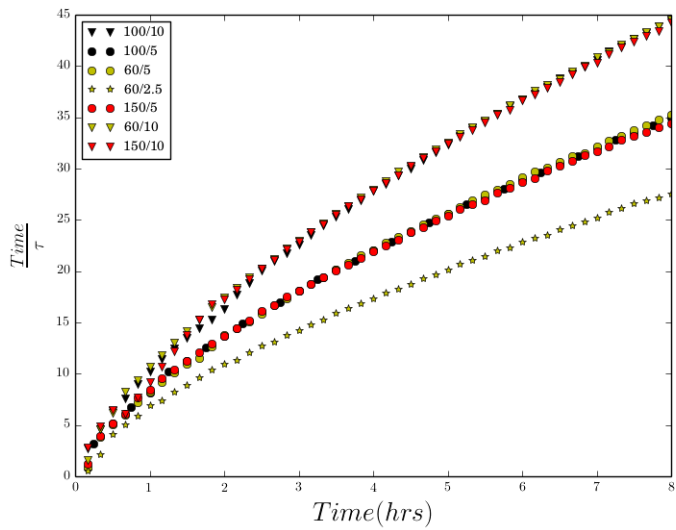


**Figure 2.2:** Plots of scaled time vs time for all runs. Scaled time is based on the convective time scale and can be thought of as the number of times an eddie has reached the top of the CBL.

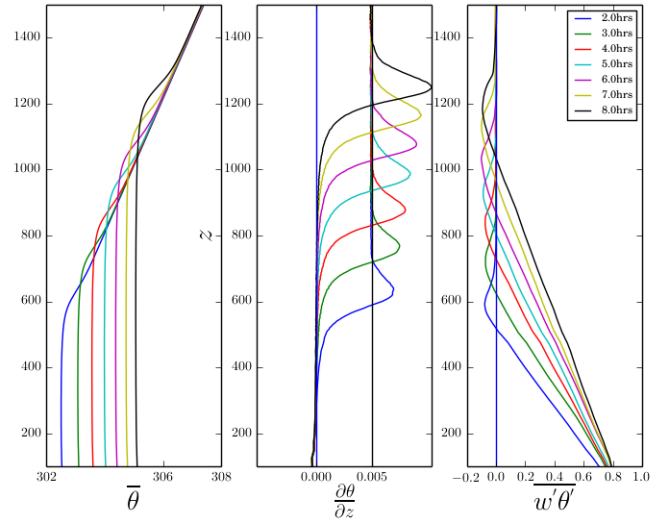


**Figure 2.3:** Vertical profiles of the ensemble and horizontally averaged potential temperature ( $\bar{\theta}$ ), its vertical gradient ( $\frac{\partial \bar{\theta}}{\partial z}$ ) and heat flux ( $\overline{w'\theta'}$ ) for the 100/5 run

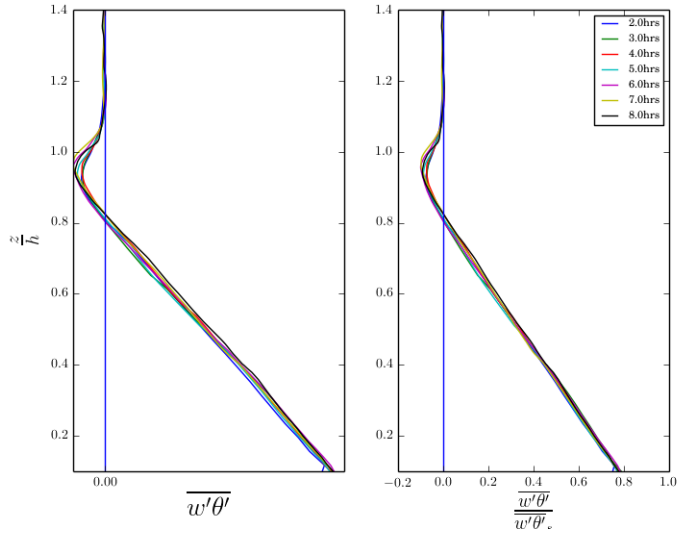


**Figure 2.4:**  $\overline{w'\theta'}$  and scaled  $\overline{w'\theta'}$  vs scaled height for the 100/5 run

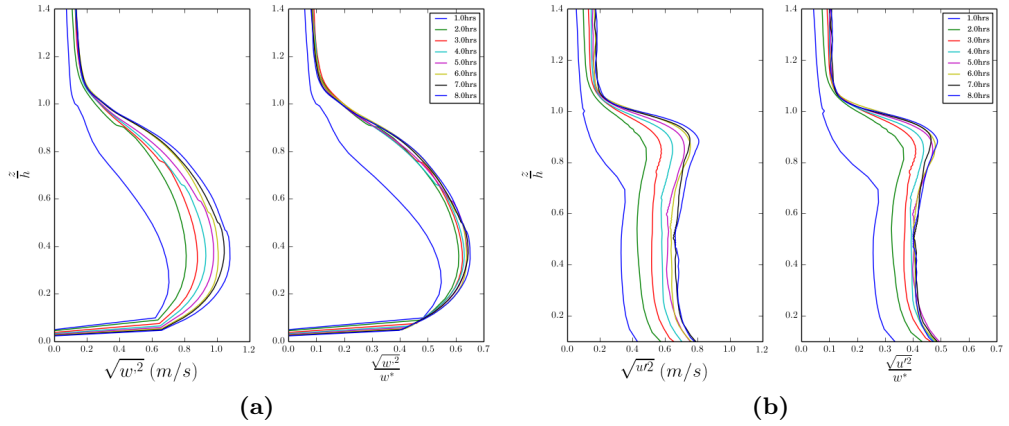


**Figure 2.5:** (a)  $\sqrt{w'^2}$  and scaled  $\sqrt{w'^2}$  vs scaled height for the 150/10 run, (b)  $\sqrt{u'^2}$  and scaled  $\sqrt{u'^2}$  vs scaled height for the 150/10 run

### 2.3.2 FFT Energy Spectra

Two dimensional FFT power spectra taken of horizontal slices of  $w'$  (??) at three different levels ( $h_0$ ,  $h$  and  $h_1$ ) are collapsed to one dimension by integrating around a semi-circle of positive wave-numbers. Isotropy in all radial directions is assumed and  $k = \sqrt{k_x^2 + k_y^2}$ . The resulting scalar density spectra show peaks in energy at the larger scales, cascading to the lower scales roughly according to a  $-\frac{5}{3}$  slope lower in the EL. At the top of the EL where turbulence is suppressed by stability, the slope is steeper. The peak in energy occur at smaller scales at  $h$  as compared to at  $h_0$ , indicating a change in the size of the dominant turbulent structures. The spectra for the horizontal turbulent velocity perturbations were similar.

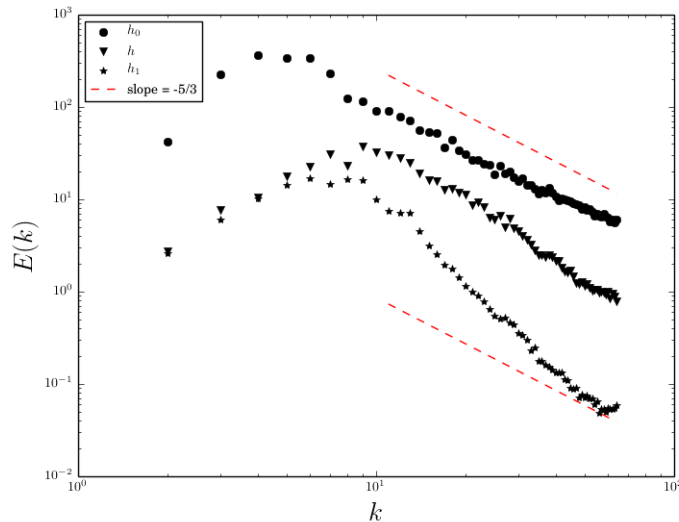


**Figure 2.6:** Scalar FFT energy vs wavenumber ( $k = \sqrt{k_x^2 + k_y^2}$ ) for the 60/2.5 run at 2 hours.  $E(k)$  is  $E(k_x, k_y)$  integrated around circles of radius  $k$ .  $E(k_x, k_y)$  is the total integrated energy over the 2D domain.  $k_x$  and  $k_y$  are number of waves per domain length.

### 2.3.3 Ensemble and horizontally averaged vertical Potential Temperature $\bar{\theta}$ and Heat Flux profiles $\overline{w'\theta'}$

The  $\bar{\theta}$  profiles exhibit an ML above which  $\frac{\partial \bar{\theta}}{\partial z} > 0$  and reaches a maximum value at  $h$  before resuming  $\gamma$  at  $h_1$  (Figures ?? and 2.7). Convective boundary layer CBL growth is stimulated by  $\overline{w'\theta'_s}$  and inhibited by  $\gamma$ .

The horizontally averaged, ensemble averaged heat flux ( $\overline{w'\theta'}$ ) profiles decrease from the surface value ( $\overline{w'\theta'_s}$ ) passing through zero to a minimum before increasing to zero (Figures ?? and 2.8). All minima are less in magnitude than the zero order approximation ( $-.2 \times \overline{w'\theta'_s}$ ) but seem to increase with increased  $\gamma$ .

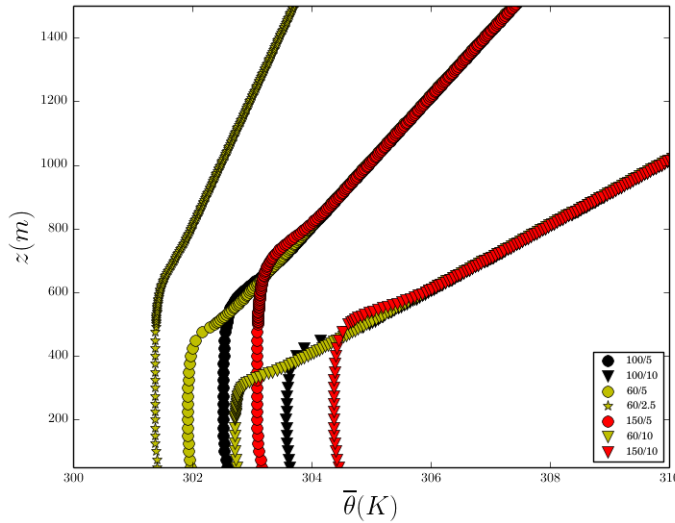


**Figure 2.7:**  $\bar{\theta}$  profiles at 2 hours

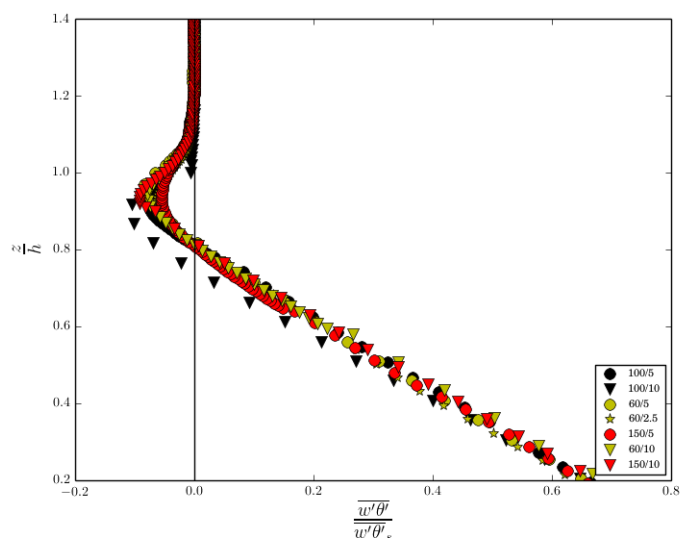


**Figure 2.8:** Scaled  $\overline{w'\theta'_s}$  profiles at 2 hours

### **2.3.4 Visualization of Structures Within the Entrainment Layer**

Horizontal slices, at the three entrainment layer (EL) levels, of the potential temperature and vertical velocity perturbations are plotted to see the turbulent structures. At the bottom of the EL ( $h_0$ ) in the 150/10 run (Figure 2.9 (a) and (d)) coherent areas of positive and negative temperature perturbations correspond to areas of upward and downward moving air.

The individual plumes of relatively cool air are more evident at the inversion ( $h$ ) and their locations correspond to areas of upward motion ((b) and (e)). Most of the upward moving cool areas are adjacent to and even encircled by smaller areas of downward moving warm air. At  $h_1$  ((c) and (f)) peaks of cool air are associated with both up and down-welling.

In the 60/2.5 run (Figure 2.10) a similar progression is evident but the impinging, cool upward moving plumes are more defined. This is to be expected since stronger stability inhibits deformation of the inversion interface.

**Figure 2.9:**  $\theta'$  (left) and  $w'$  (right) at 2 hours at  $h_0$  (a,d),  $h$  (c,e) and  $h_1$  (d,f)

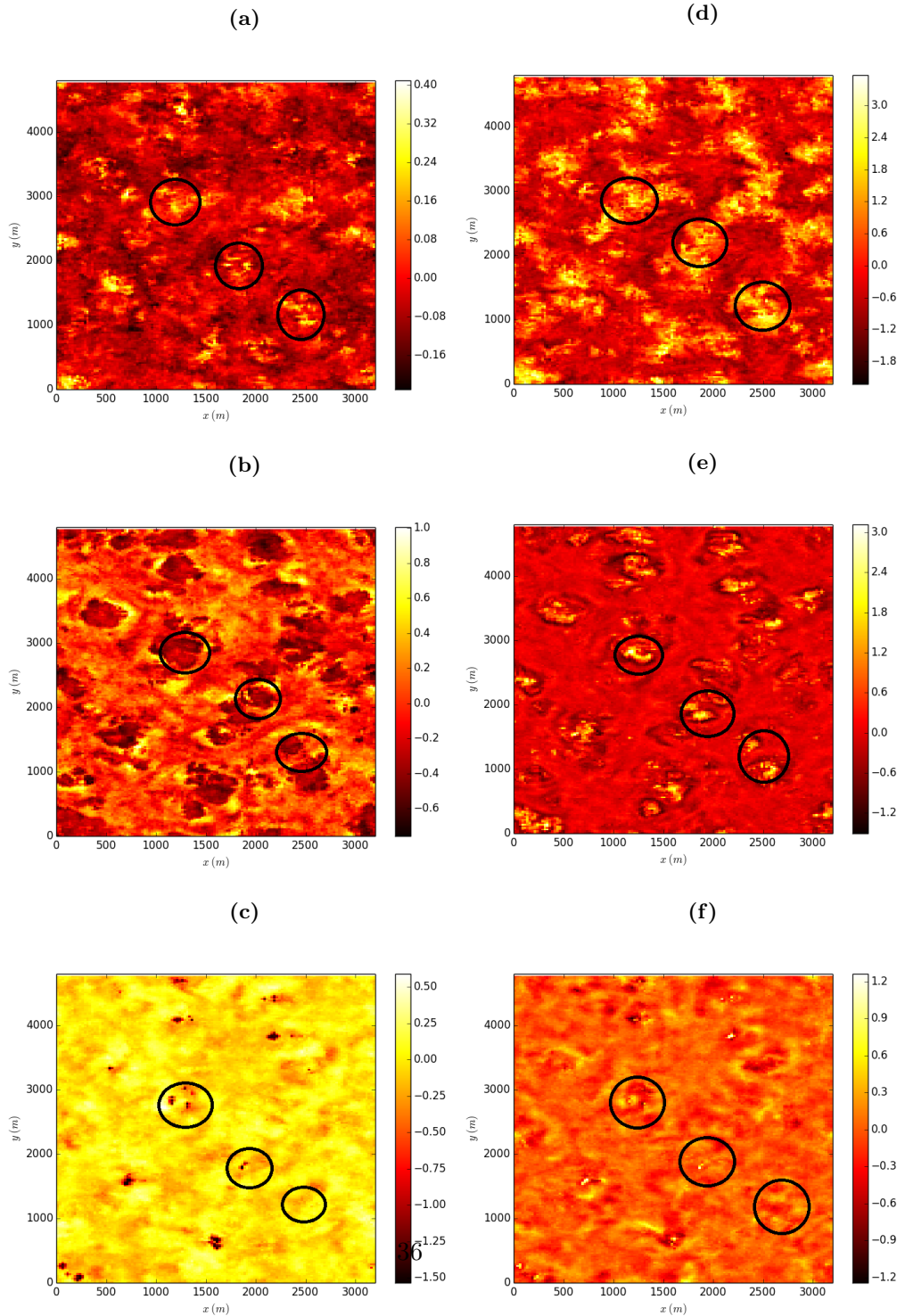
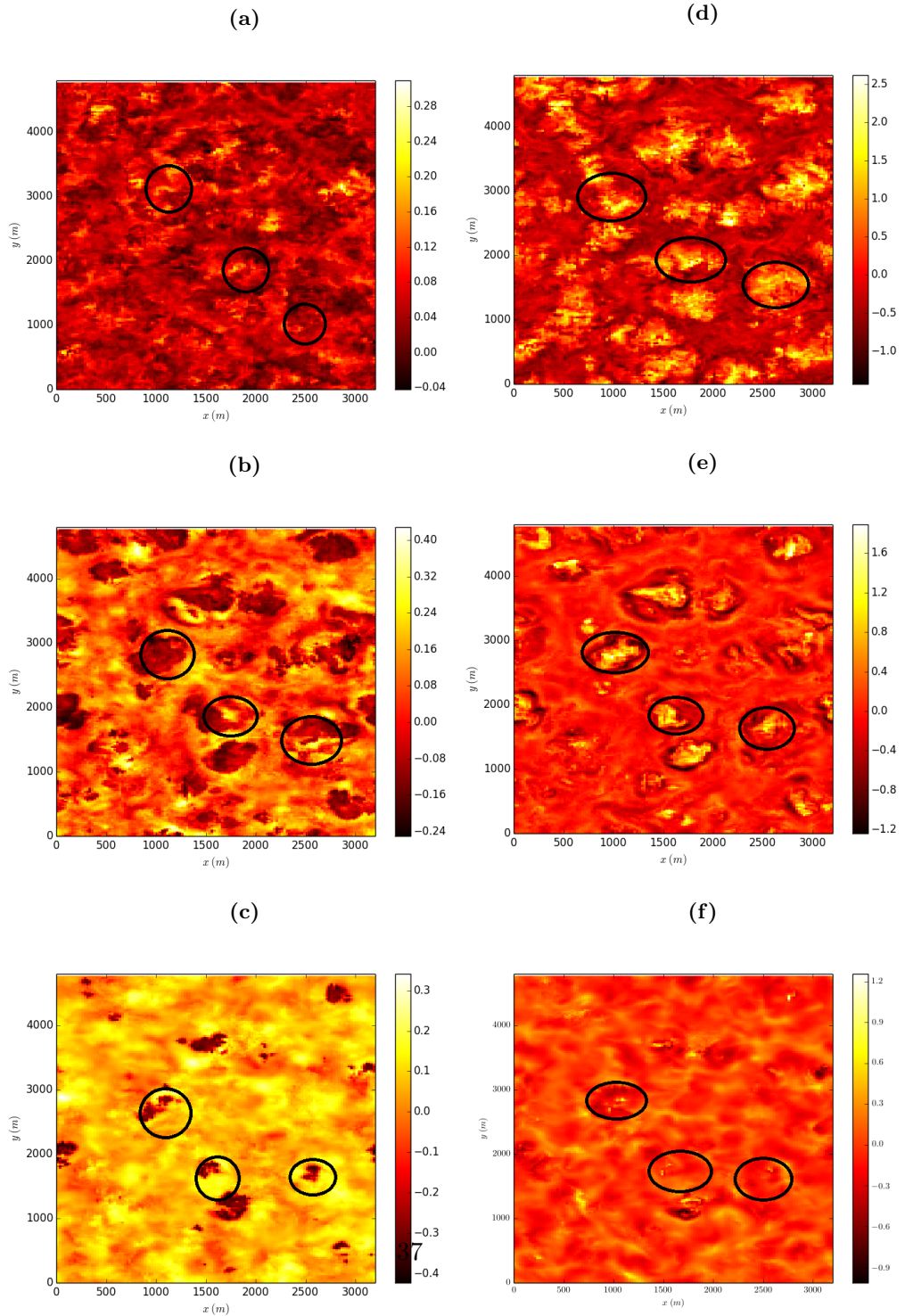


**Figure 2.10:**  $\theta'$  (left) and  $w'$  (right) at 2 hours at  $h_0$  (a,d),  $h$ (b,e) and  $h_1$ (c,f)



## 2.4 Local Mixed Layer Heights ( $h_0^l$ )

Local  $\theta$  profiles (Figures 2.11 and 2.12) exhibit a distinct ML before resuming  $\gamma$  but not always a clearly defined EL. There are sharp changes in the profile well into the free atmosphere, due possibly to waves, which render the gradient method for determining  $h^l$  unusable. Instead a linear regression method is used, whereby three lines representing: the ML, the EL and the upper lapse rate ( $\gamma$ ), are fit to the profile according to the minimum residual sum of squares (RSS). Determining local ML height ( $h_0^l$ ) was more straight forward than the local height of maximum potential temperature gradient ( $h^l$ ) for the reasons stated above.

Figure 2.11 shows two local  $\theta$  profiles where  $h_0^l$  is relatively high. A sharp interface is evident indicating that this is within an active plume impinging on the stable layer. In Figure 2.12 where  $h_0^l$  is relatively low a less defined interface indicates a point now outside a rising plume. Contour plots (Figure 2.13) show regions of high  $h_0^l$  corresponding to regions of upward moving relatively cool air at  $h$ .

The distribution of  $h_0^l$  is related to the depth of the entrainment layer (EL). Spread increases with increasing  $\overline{w'\theta'_s}$  and decreases with increasing  $\gamma$  (Figure 2.14). When scaled by  $h$  (Figure 2.15), the local ML height distribution has spread that narrows with increased  $\gamma$  and seems relatively uninfluenced by change in  $\overline{w'\theta'_s}$ . The upper limit seems to be constant at about 1.1( $\times h$ ), whereas the lower limit varies depending on  $\gamma$ . Runs with lower  $h$  and narrower  $\Delta h$  have relatively larger spacing between bins and so higher numbers in each bin. The above supports the results outlined in Section 2.6.1.

Local  $\theta$  profiles (Fig. ??) exhibit a distinct ML before resuming  $\gamma$  but not a clearly defined EL. There are sharp changes in the profile well into the free atmosphere, due possibly to waves, which render the gradient method for determining  $h^l$  unusable. Instead a linear regression method is used, whereby three lines representing: the mixed layer (ML), the EL and the

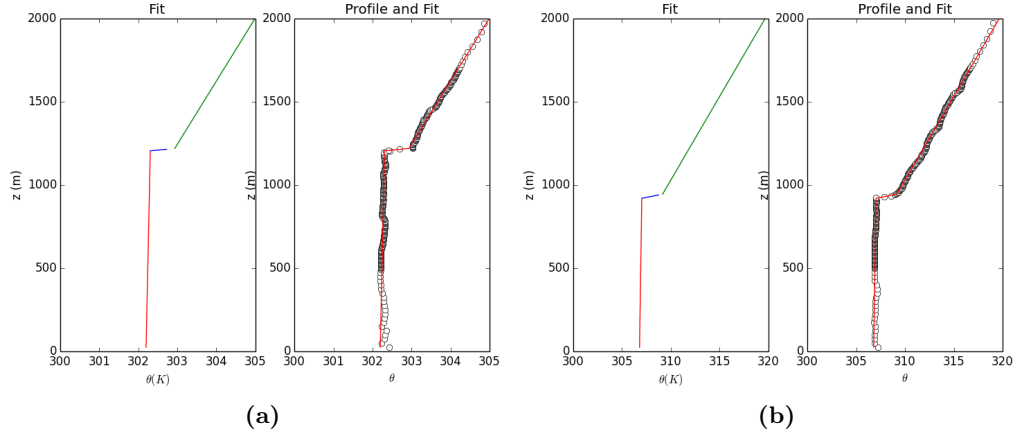


**Figure 2.11:** Local vertical  $\theta$  profiles with 3-line fit for the 60/2.5 (a) and 150/10 (b) runs at points where  $h_0^l$  is high.

upper lapse rate ( $\gamma$ ) are fit to the profile according to the minimum residual sum of squares (RSS). Determining local ML height ( $h_0^l$ ) was more straight forward than the local height of maximum potential temperature gradient  $h^l$  for the reasons stated above.

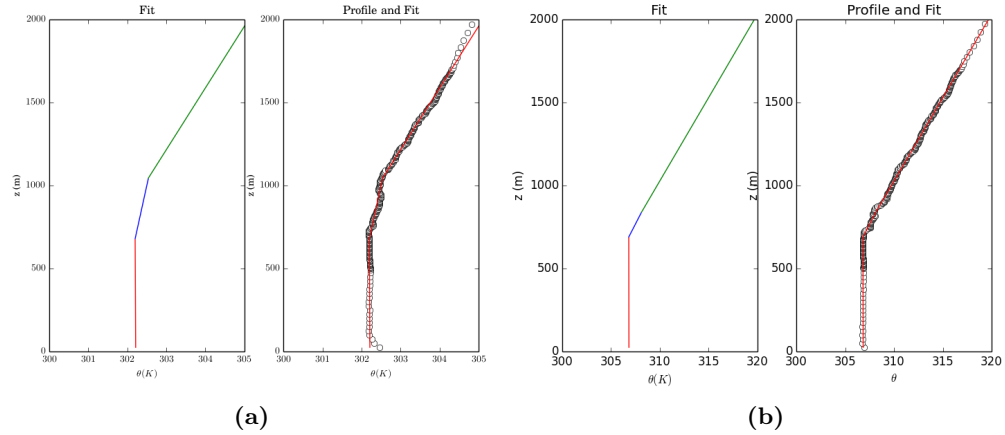


**Figure 2.12:** Local vertical  $\theta$  profiles with 3-line fit for the 60/2.5 (a) and 150/10 (b) runs at points where  $h_0^l$  is low.

**Figure 2.13:**  $\theta'$  (a,d),  $w'$  (b,e) at  $h_1$ (c,f) and local ML height  $h_0^l$  at 2 hours for 60/2.5 (left) and 150/10 (right) runs

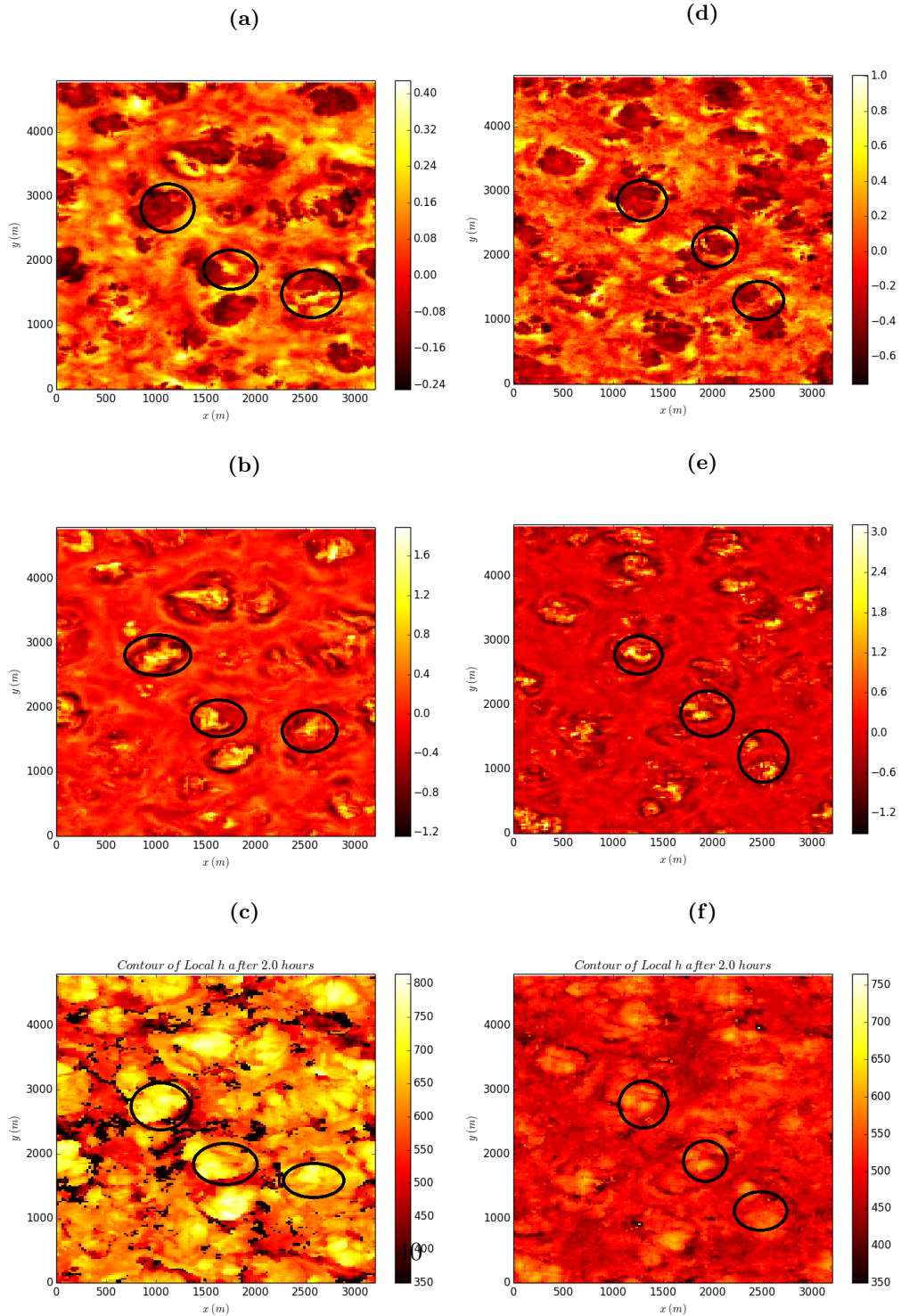


**Figure 2.14:** Histograms of  $h_0^l$  for  $\overline{w'\theta'_s} = 150$  to 60( $W/m^2$ ) (a to c) and  $\gamma = 10$  to 2.5( $K/Km$ ) (c to g) at 5 hours

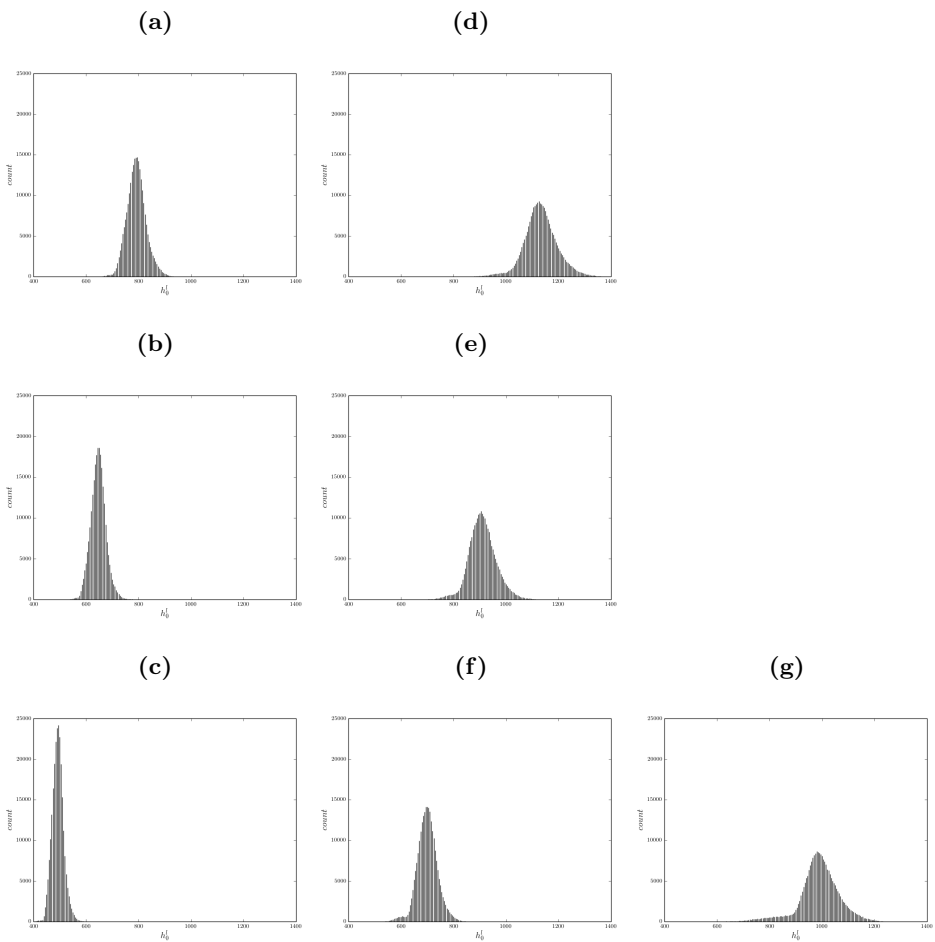
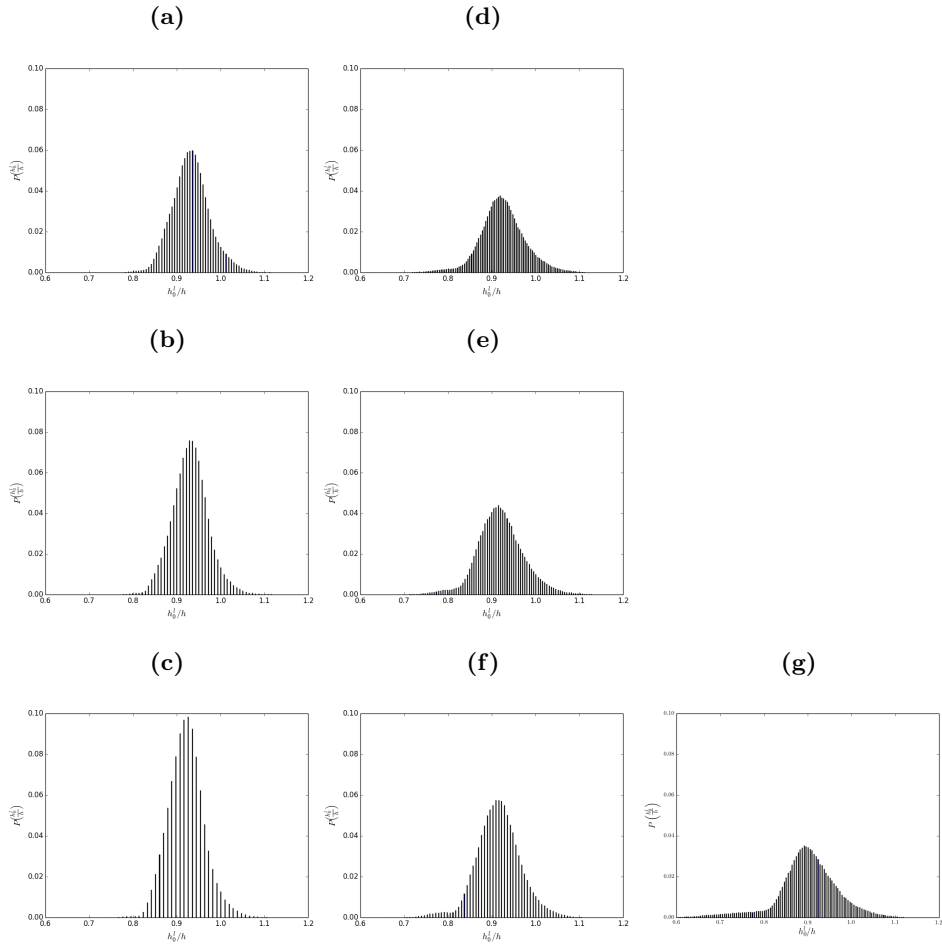


**Figure 2.15:** PDFs of  $\frac{h_0^l}{h}$  for  $\overline{w'\theta'_s} = 150$  to  $60(W/m^2)$  (a to c) and  $\gamma = 10$  to  $2.5(K/Km)$  (c to g) at 5 hours



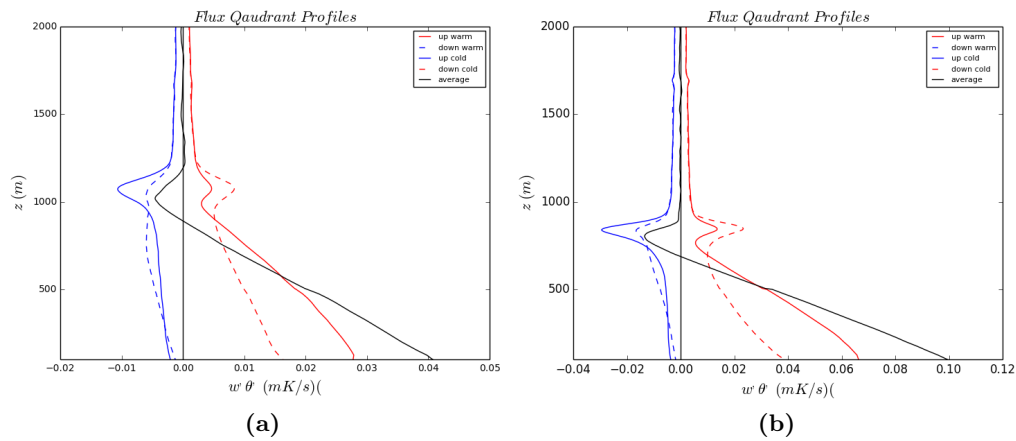
## 2.5 Flux Quadrants

As Sullivan et al. point out in [23] when broken out into four quadrants (Figure 2.16) the  $\overline{w'\theta'}$  profiles have upper extrema above that of the total average profile ( $z_f$ ). 2D histograms of the four quadrants are plotted at  $h_0$ ,  $h$  and  $h_1$  to see how the distributions are influenced by changes in  $\overline{w'\theta'}$  and  $\gamma$ .

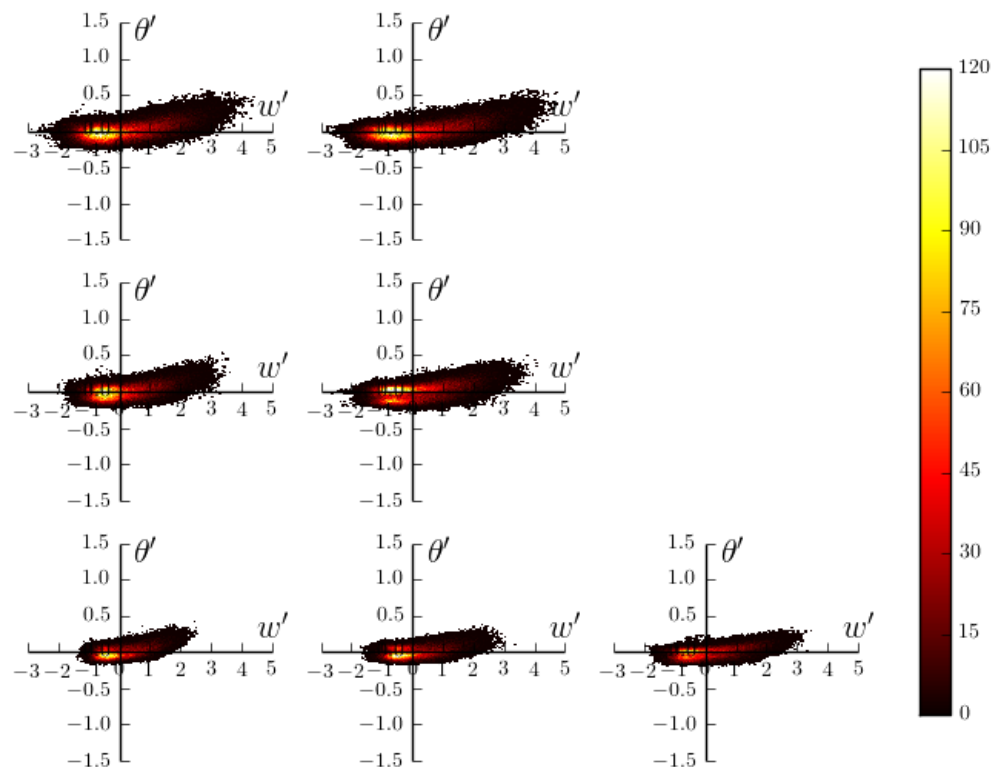
At  $h_0$  (Figure ??) fast updraughts are relatively warm. The spread in  $w'$  increases with increasing  $\overline{w'\theta'_s}$  and decreases with increased  $\gamma$ . At  $h$  (Figure 2.16) the faster updraughts are now relatively cool and movement (both up and down) of warmer air from aloft becomes more prominent. The spread of  $w'$  and  $\theta'$  both increase with increasing  $\overline{w'\theta'}$  whereas that of  $\theta'$  increases only slightly with increased stability. As expected stability inhibits both upward and downward  $w'$ .

Although the quadrant of overall largest magnitude is that of upward moving cool air, Sullivan et al.'s assertion in [23] that in the EL the heat flux is effectively due to downward moving warm air because the other three quadrants cancel, is found to be approximately true. At the top of the EL (Figure 2.22) velocities are damped and the distributions approach symmetry apart from some slow, cool, impinging up- and down-draughts as in Figure 2.13.

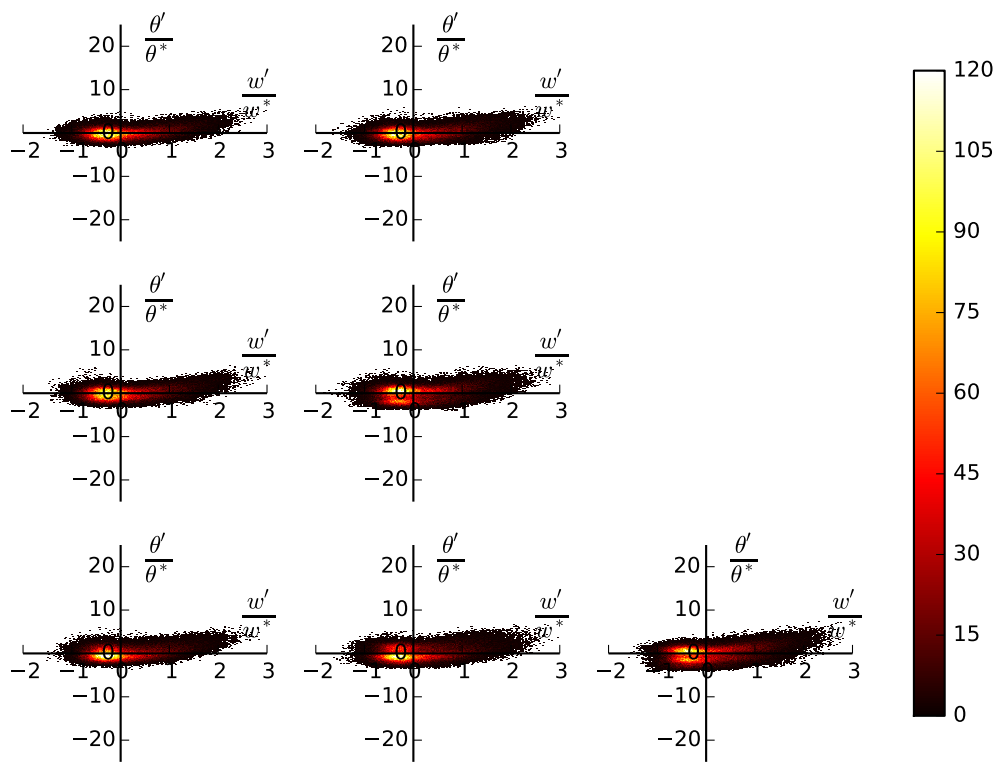
2D Histograms of the four quadrants are plotted at  $h_0$ ,  $h$  and  $h_1$  (based on the averaged  $\theta$  profiles) to visualize how the distributions are influenced by changes in  $\overline{w\cdot\theta}$  and  $\gamma$ . At  $h_0$  (Fig. ??) fast updraughts are relatively warm and are inhibited by increasing upper stability. The spread in velocity increases with increasing  $\overline{w\cdot\theta_s}$



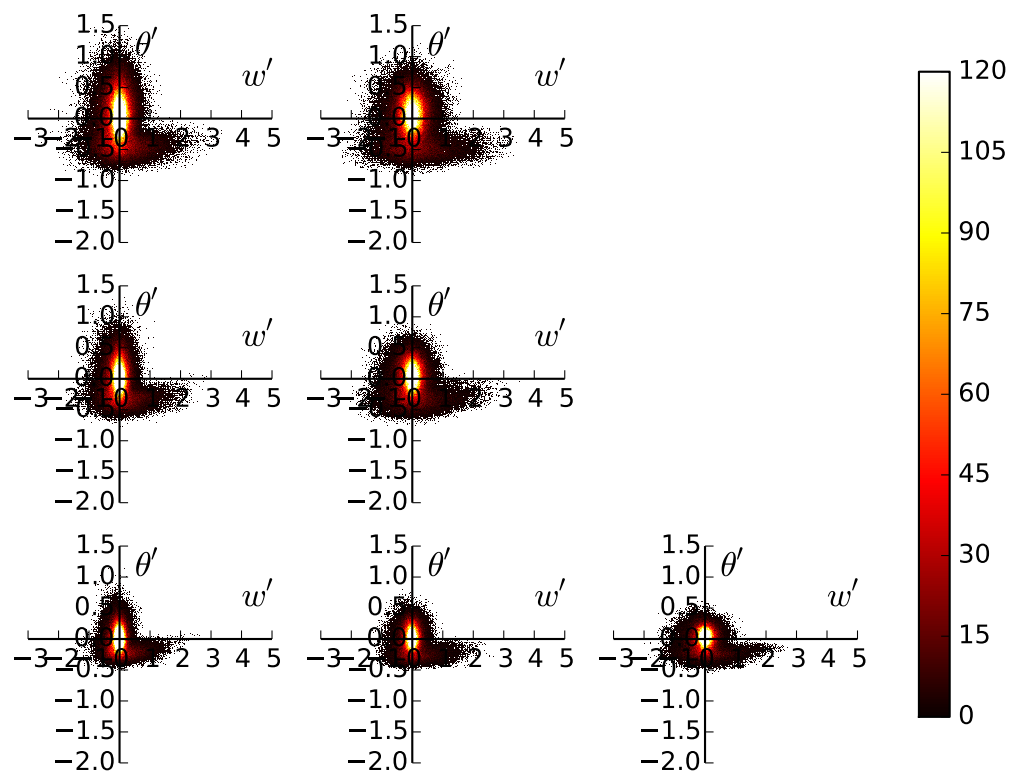
**Figure 2.16:** Scaled  $\overline{w'\theta'}$  quadrant profiles at 5 hours for the 60/2.5 (a) and 150/10 (b) run



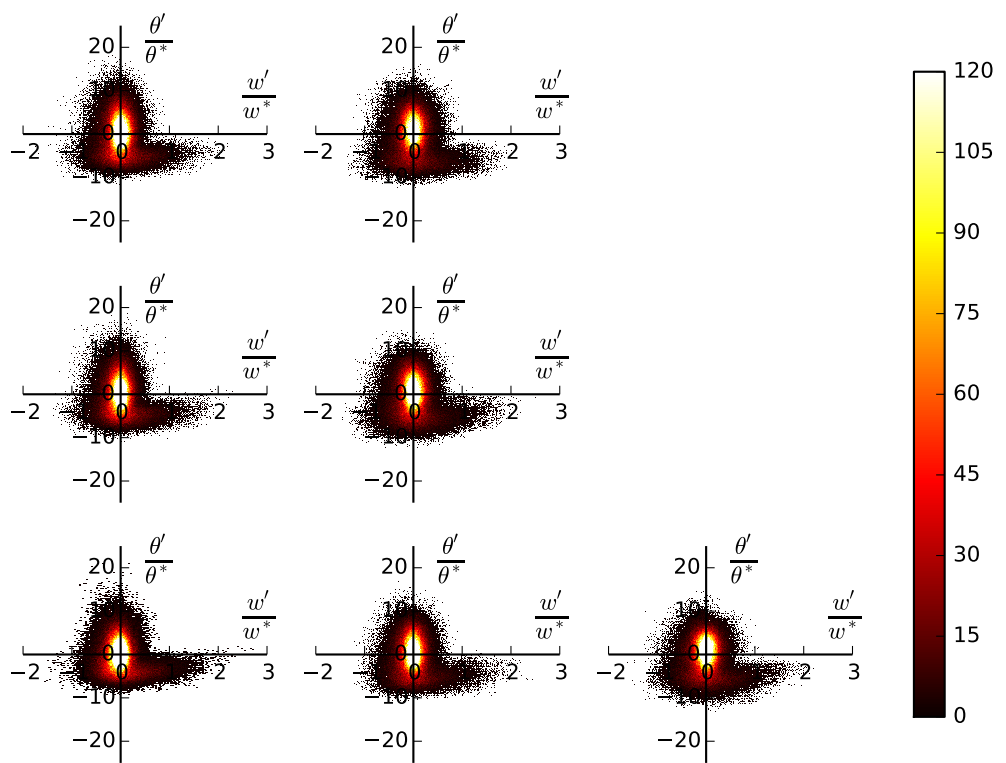
**Figure 2.17:**  $\overline{w'\theta'}$  quadrants at  $h_0$  for  $w'\theta' = 150 - 60$  (W/m<sup>2</sup>) (top-bottom) and  $\gamma = 10 - 2.5$  (K/Km) (left-right) at 5 hours



**Figure 2.18:**  $\overline{w'\theta'}$  quadrants at  $h_0$  for  $w'\theta' = 150 - 60(W/m^2)$  (top-bottom) and  $\gamma = 10 - 2.5(K/Km)$  (left-right) at 5 hours

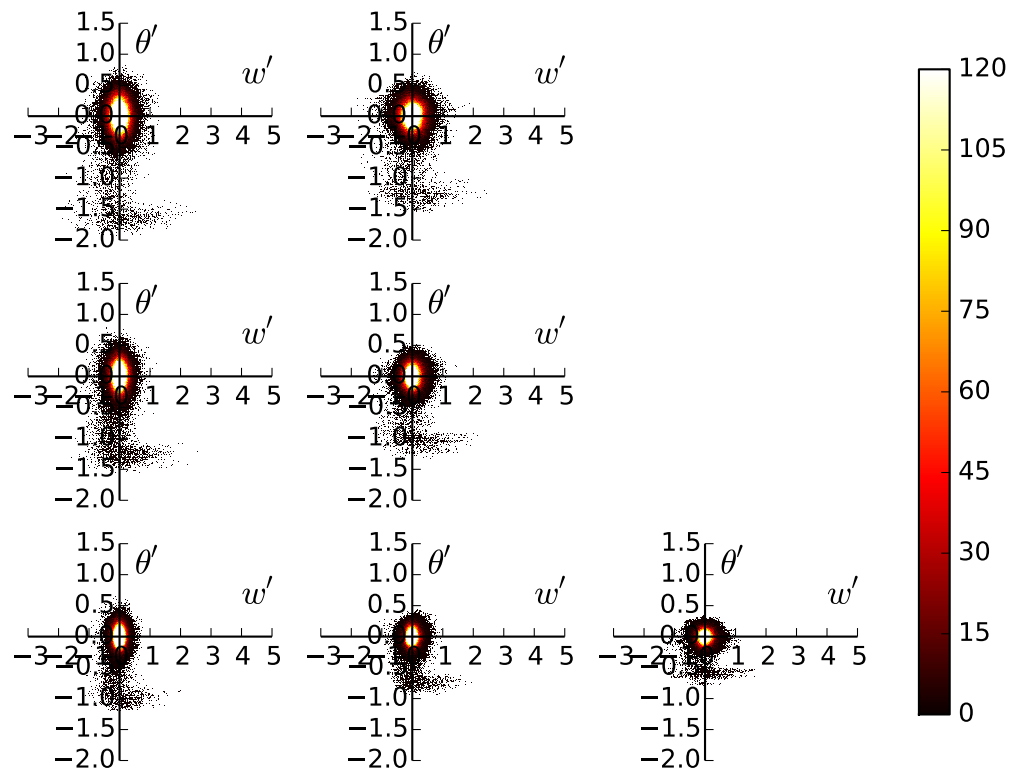


**Figure 2.19:**  $\overline{w'\theta'}$  quadrants at  $h$  for  $w'\theta' = 150 - 60(\text{W}/\text{m}^2)$  (top - bottom) and  $\gamma = 10 - 2.5(\text{K}/\text{Km})$  (left - right) at 5 hours

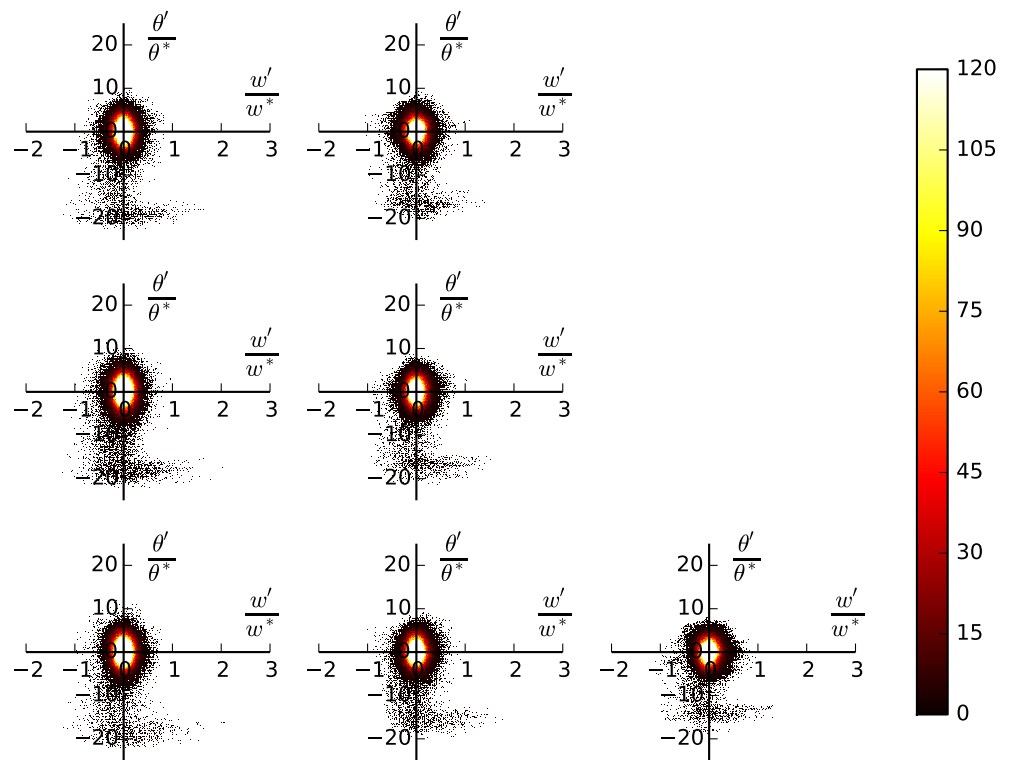


**Figure 2.20:**  $\overline{w'\theta'}$  quadrants at  $h$  for  $w'\theta' = 150 - 60(\text{W}/\text{m}^2)$  (top - bottom) and  $\gamma = 10 - 2.5(\text{K}/\text{Km})$  (left - right) at 5 hours

**Figure 2.21:**  $\overline{w'\theta'}$  quadrants at  $h_1$  for  $w'\theta' = 150$  to 60( $\text{W}/\text{m}^2$ ) (top to bottom) and  $\gamma = 10$  to 2.5( $\text{K}/\text{Km}$ ) (left to right) at 5 hours



**Figure 2.22:**  $\overline{w'\theta'}$  quadrants at  $h_1$  for  $w'\theta' = 150$  to 60( $\text{W}/\text{m}^2$ ) (top to bottom) and  $\gamma = 10$  to 2.5( $\text{K}/\text{Km}$ ) (left to right) at 5 hours



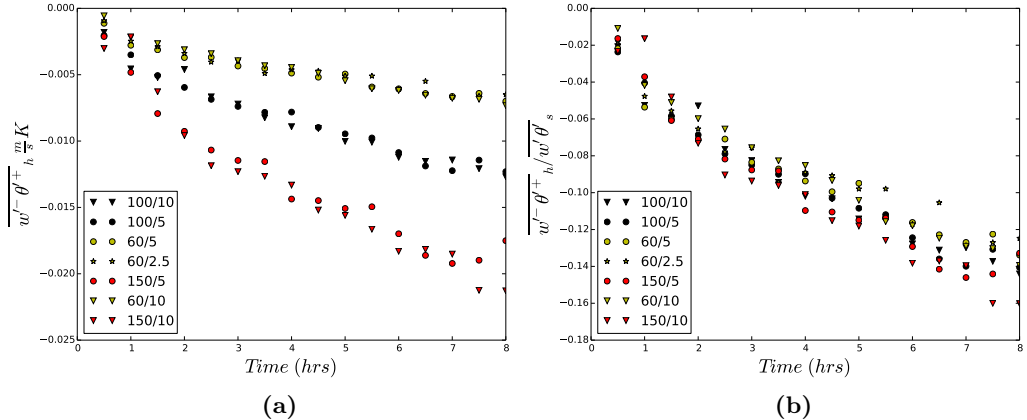


**Figure 2.23:** Plots of (a) the average downward moving warm air at  $h$  ( $\overline{w' - \theta'}^+_h$ ) and (b)  $\overline{w' - \theta'}^+_h$  scaled by the average vertical heat flux  $\overline{w' \theta'}_s$  vs time

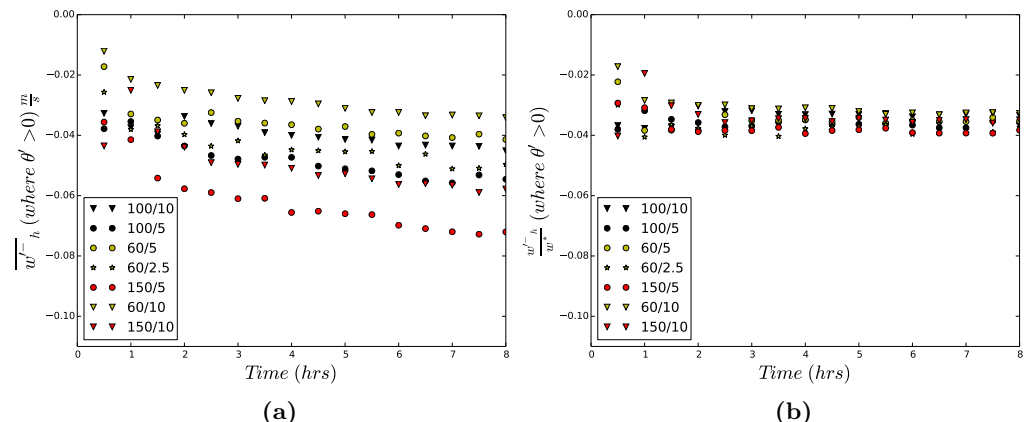


**Figure 2.24:** Plots of (a) the average negative vertical turbulent velocity perturbation  $w'^-$  at points where the turbulent  $\theta'$  perturbation is positive ( $\theta' > 0$ ) (b)  $w'^-$  where  $\theta' > 0$  scaled by  $w^*$ .

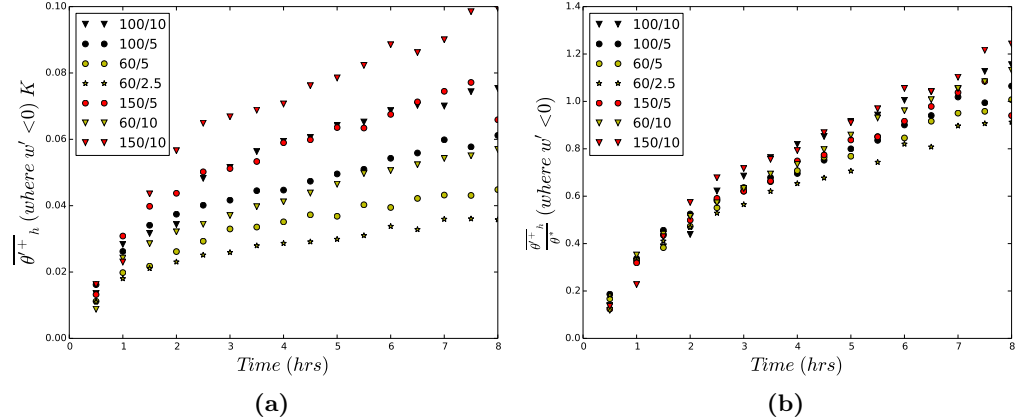


**Figure 2.25:** Plots of (a) the average positive potential temperature perturbation  $\theta'^+$  at points where the turbulent vertical velocity perturbation is negative ( $w' < 0$ ) (b)  $\theta'^+$  where  $w' < 0$  scaled by  $\theta^*$ .

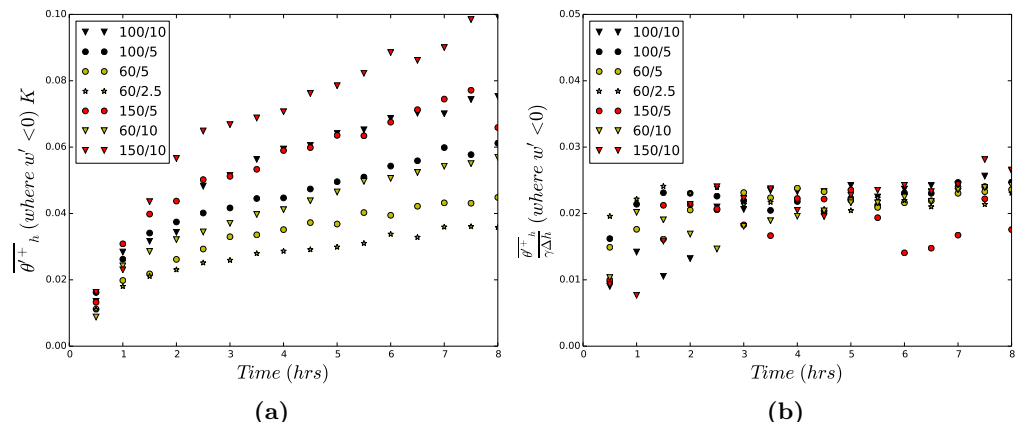


**Figure 2.26:** Plots of (a) the average positive potential temperature perturbation  $\theta'^+$  at points where the turbulent vertical velocity perturbation is negative ( $w' < 0$ ) (b)  $\theta'^+$  where  $w' < 0$  scaled by  $\gamma\Delta h$ .

## 2.6 $h$ and $\Delta h$ based on Average Profiles

git

### 2.6.1 $\frac{\Delta h}{h}$ vs $Ri^b$

The scaled upper EL limits ( $\frac{h_1}{h}$ ) collapse well in Figure 2.27 to an initial value of approximately 1.15, decreasing to about 1.1.  $\frac{h_0}{h}$ s appear grouped according to  $\gamma$  and increase with respect to time. So overall the scaled EL appears to narrow with time. The scaled flux based EL ( $z_{f0}$  and  $z_{f1}$ ) appears to remain constant with respect to time in Figure 2.28.

The lower entrainment layer limit  $h_0$  is the point at which the vertical  $\frac{\partial \bar{\theta}}{\partial z}$  exceeds a threshold (.0002) chosen such that it is positive, and at least an order of magnitude smaller than  $\gamma$ . Although the resulting scaled EL depth decreases with increasing Ri grouping according to  $\gamma$  is evident in Figure 2.30.

To explore how varying the threshold value affects the relationship between scaled EL depth and Richardson number (Ri), plots analogous to Figure 2.30 were produced at two additional thresholds. A higher threshold value (.0004) results in a higher  $h_0$  (Figure 2.31) and so a narrower EL but a similar grouping according to  $\gamma$  (Figure 2.32). A lower threshold value (.0001) results in a lower  $h_0$  (Figure 2.33) but also similar grouping according to  $\gamma$  (Figure 2.34).

When the height definitions are based on the scaled vertical  $\frac{\partial \bar{\theta}}{\partial z}$  i.e.  $\frac{\partial \bar{\theta}}{\partial z}/\gamma$  profile, only  $h_0$  changes and for clarity we call this EL depth  $\Delta h^*$  and the revised Richardson number  $Ri^*$ . The curves now collapse and scaled EL depth is seen to decrease with increasing  $Ri^*$  (Figures 2.35 to 2.37).

There is a slight collapsing effect on the scaled entrainment rate vs Ri relationship when the heights are defined based on the scaled vertical potential temperature gradient  $\frac{\partial \bar{\theta}}{\partial z}/\gamma$  profile in Figure ??.

bg

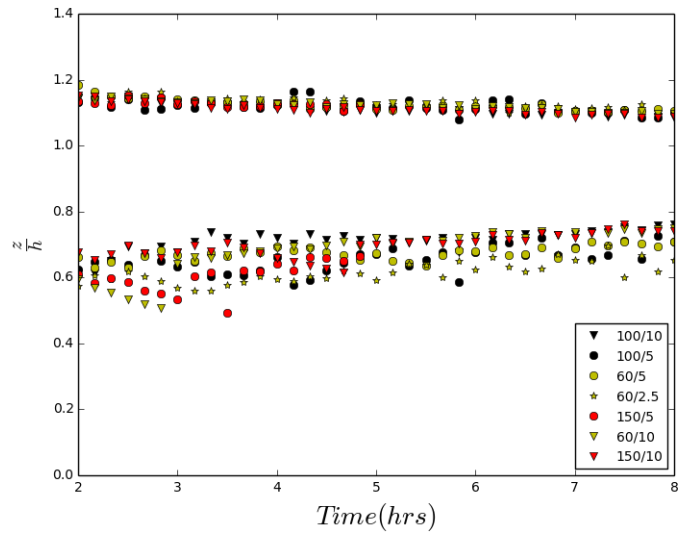


**Figure 2.27:** Scaled Entrainment Layer limits ( $\frac{h_1}{h}$  and  $\frac{h_0}{h}$ ) vs time

### 2.6.2 $\frac{w_e}{w^*}$ vs $Ri^{-1}$

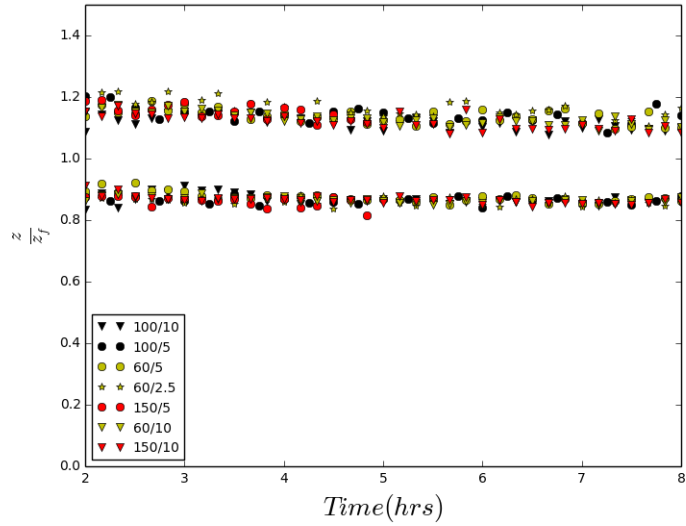


**Figure 2.28:** Scaled Entrainment Layer limits ( $z_{f1}$  and  $z_{f0}$ ) vs time

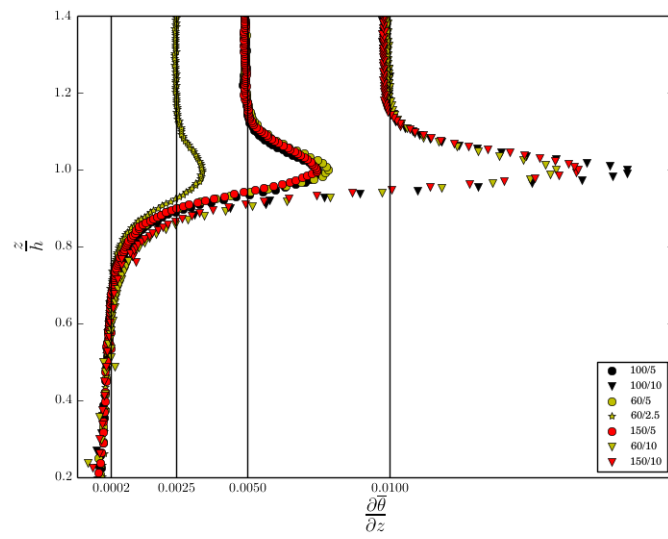


**Figure 2.29:** Vertical  $\frac{\partial \bar{\theta}}{\partial z}$  profiles with threshold at .0002

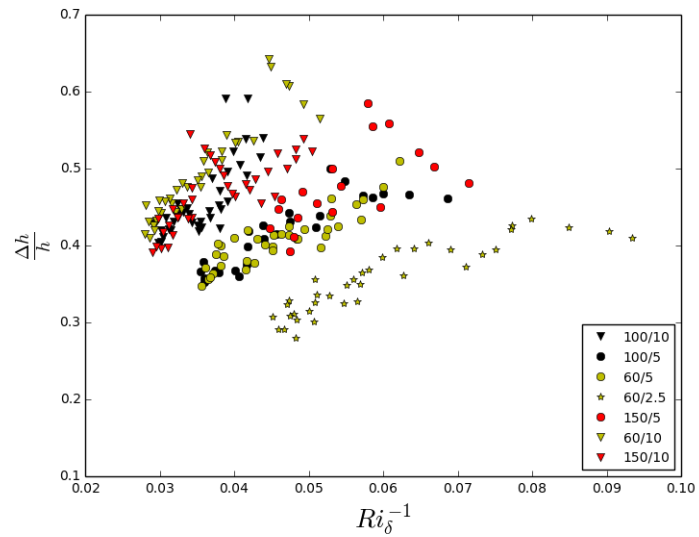


**Figure 2.30:** Scaled EL depth vs inverse bulk Richardson Number with threshold at .0002

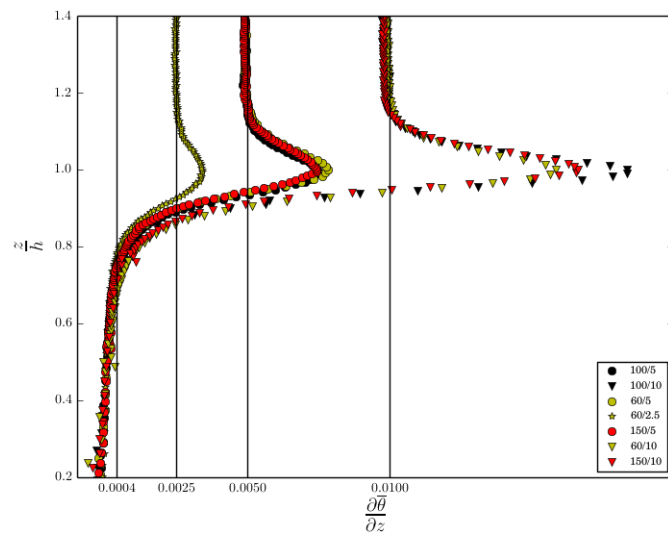


**Figure 2.31:** Vertical  $\frac{\partial \bar{\theta}}{\partial z}$  profiles with threshold at .0004

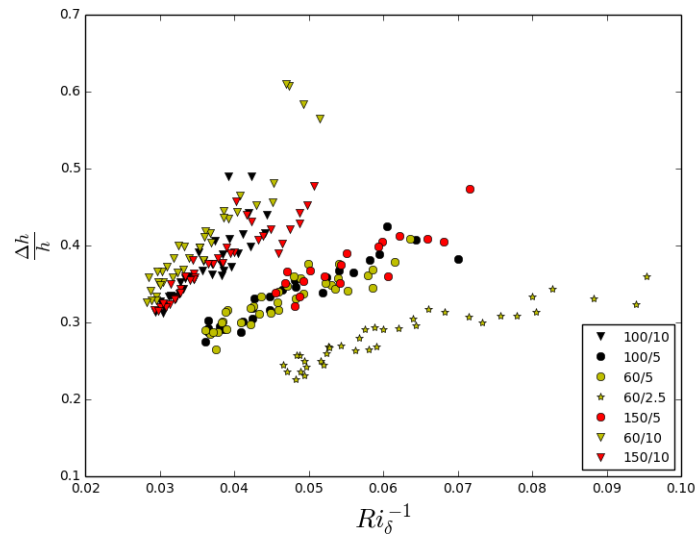


**Figure 2.32:** Scaled EL depth vs inverse Richardson Number with threshold at .0004

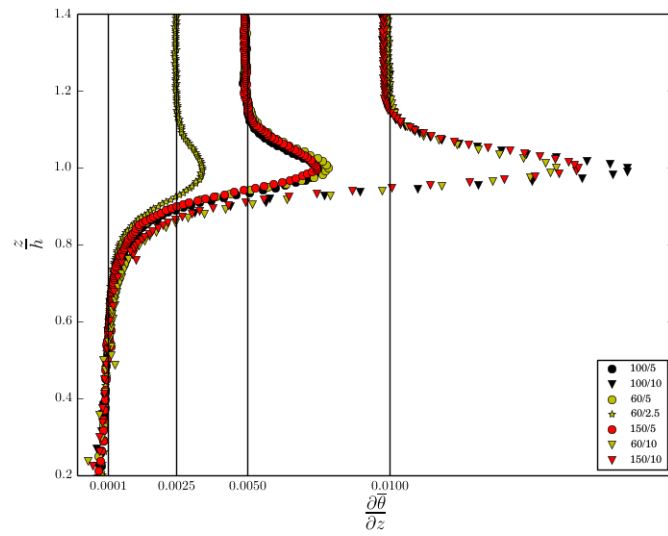


**Figure 2.33:** Vertical  $\frac{\partial \bar{\theta}}{\partial z}$  profiles with threshold at .0001

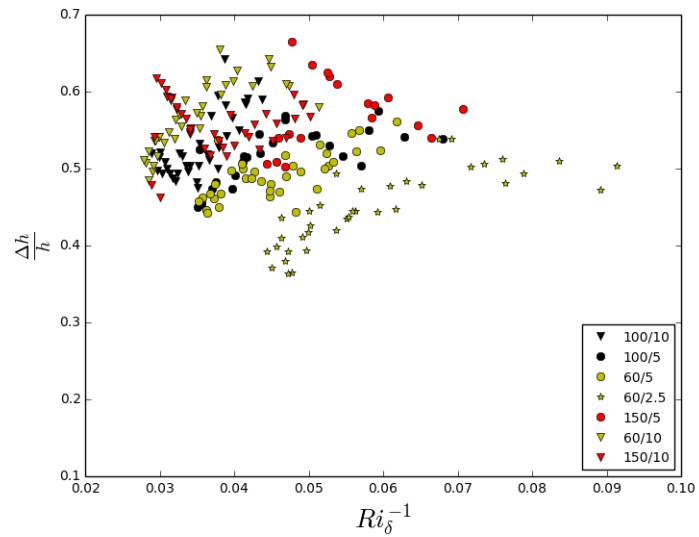


**Figure 2.34:** Scaled EL depth vs inverse bulk Richardson Number with threshold at .0001

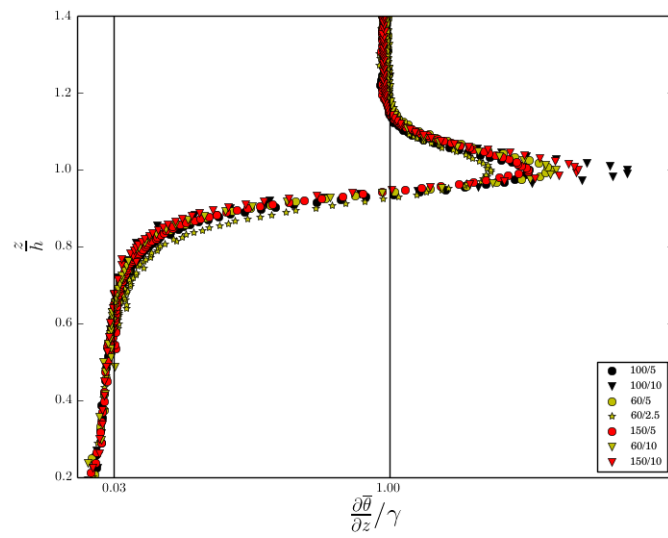


**Figure 2.35:** Scaled vertical  $\frac{\partial \bar{\theta}}{\partial z}$  profiles with threshold at .03

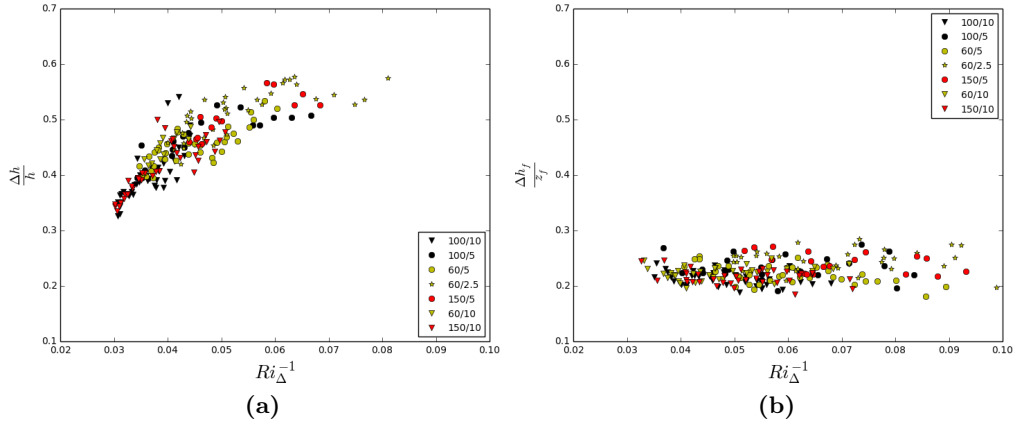


**Figure 2.36:** Plots of scaled EL depth vs  $Ri^{-1}$  with CBL height. EL limits and so  $\Delta\theta$  based on the  $\frac{\partial\bar{\theta}}{\gamma}$  in (a) and the  $\frac{\bar{w}'\bar{\theta}'}{w'\theta'_s}$  profile in (b).

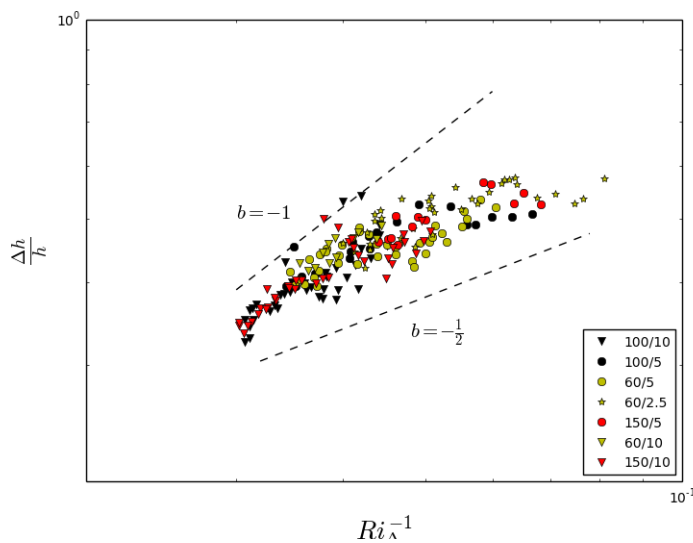


**Figure 2.37:** Scaled EL depth vs  $Ri^{-1}$  based on the  $\frac{\partial\bar{\theta}}{\gamma}$  profile in log-log coordinates to see likely values of the exponent  $b$

Covective Boundary Layer (CBL) height ( $h$ ) (Fig. 2.39) grows rapidly initially with a steadily decreasing rate and is a linear function of scaled time (Fig. ??).

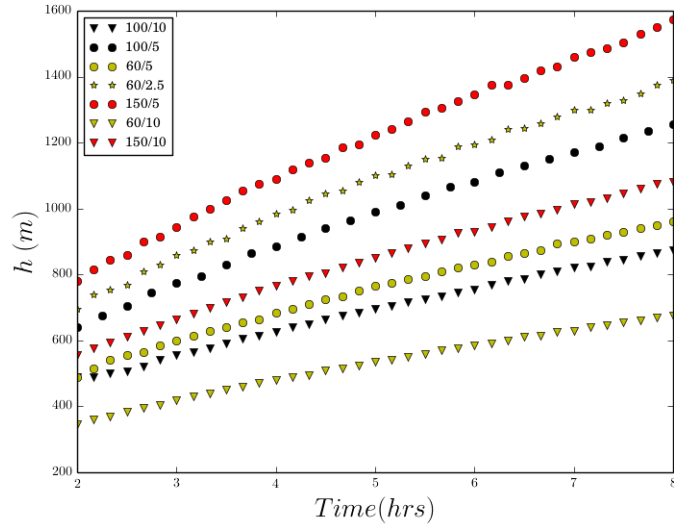


**Figure 2.38:**  $h$  vs time for all runs

Inverse Richardson Numbers ( $Ri^{-1}$ ) (bulk  $Ri: = \frac{gh}{\theta_{ML}} \frac{\Delta\theta}{w^{*2}}$ ,  $\Delta\theta = \bar{\theta}(h_1) - \bar{\theta}(h_0)$  and gradient  $Ri: = \frac{g}{\theta_{ML}} \frac{\gamma h^2}{w^{*2}}$ ) decrease with respect to time, clustering according to  $\gamma$ . (Fig. 2.41)

The entrainment rate ( $w_e = \frac{dh}{dt}$ ) is determined from the slope of a second order polynomial fit to  $h(\text{time})$  (Fig. 2.39). When scaled by ( $w^*$ ) it is a roughly linear function of the bulk  $Ri^{-1}$ , whereas it is asymptotic to a linear function of the gradient  $Ri^{-1}$ . (Fig. ??)

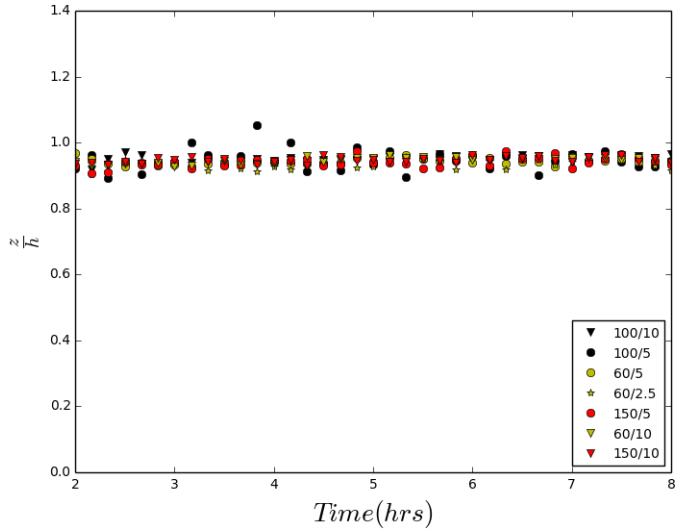


**Figure 2.39:**  $\frac{z_f}{h}$  vs Time

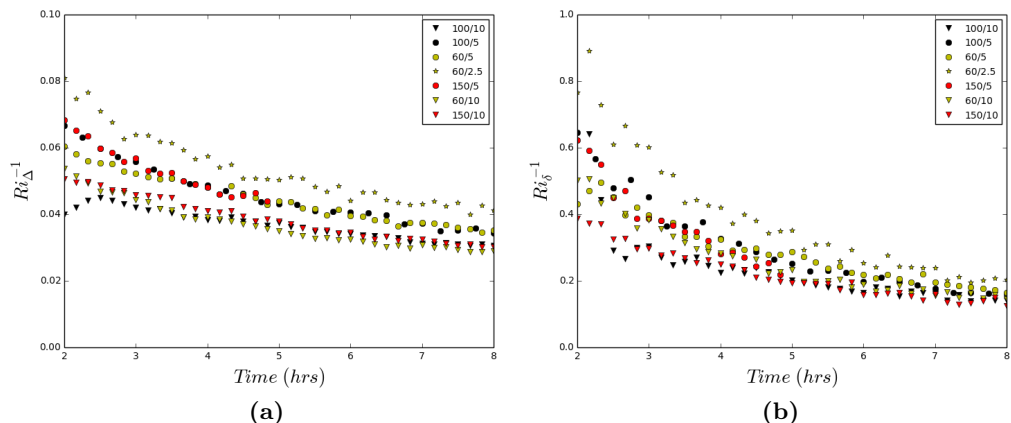


**Figure 2.40:** Inverse Richardson number vs time based on the  $\frac{\partial \bar{\theta}}{\partial z}$  profile using  $\Delta h$  across the EL in (a) and  $\delta\theta$  at  $h$  in (b) (2.2)

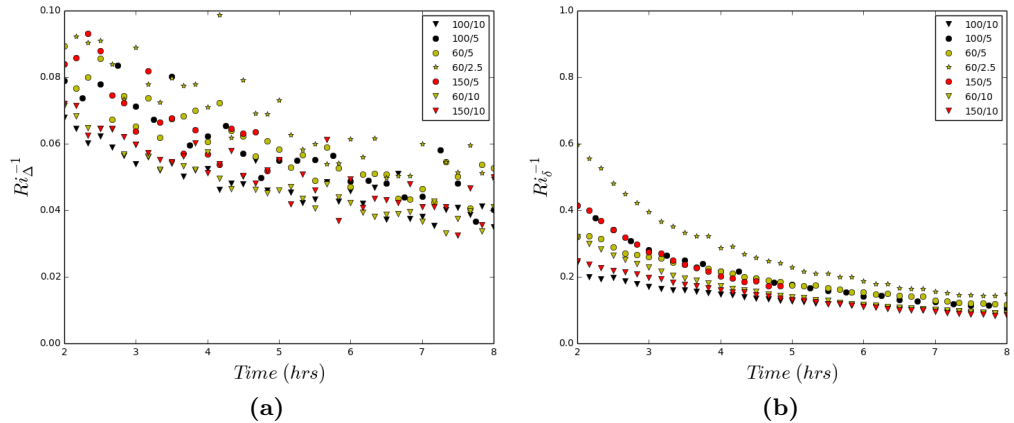


**Figure 2.41:** Inverse Richardson number vs time based on the  $\frac{\overline{w' \theta'}}{\overline{w'} \overline{\theta_s'}}$  profile using  $\Delta h$  across the EL in (a) and  $\delta \theta$  at  $z_f$  in (b) (2.1)

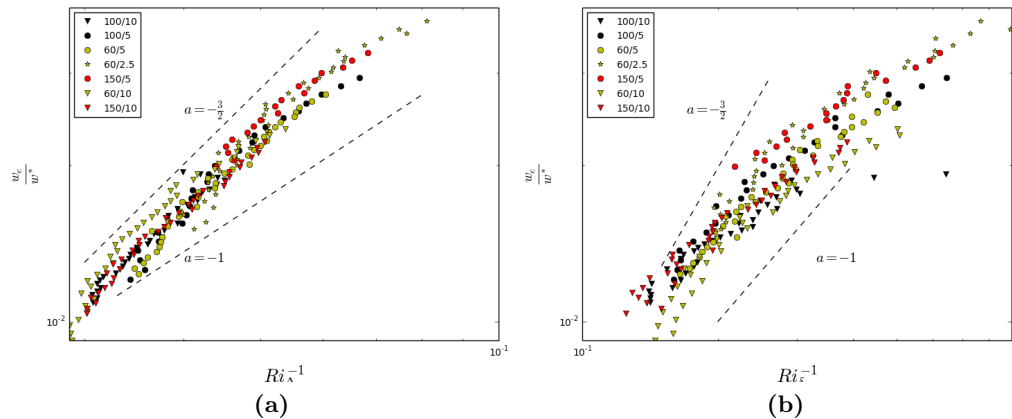


**Figure 2.42:** Scaled entrainment rate vs inverse Richardson number ( $Ri^{-1}$ ), where  $Ri$  is based on the  $\frac{\partial\bar{\theta}}{\partial z}$  profile using  $\Delta h$  accross the EL in (a) and  $\delta\theta$  at  $h$  in (b) (2.1)

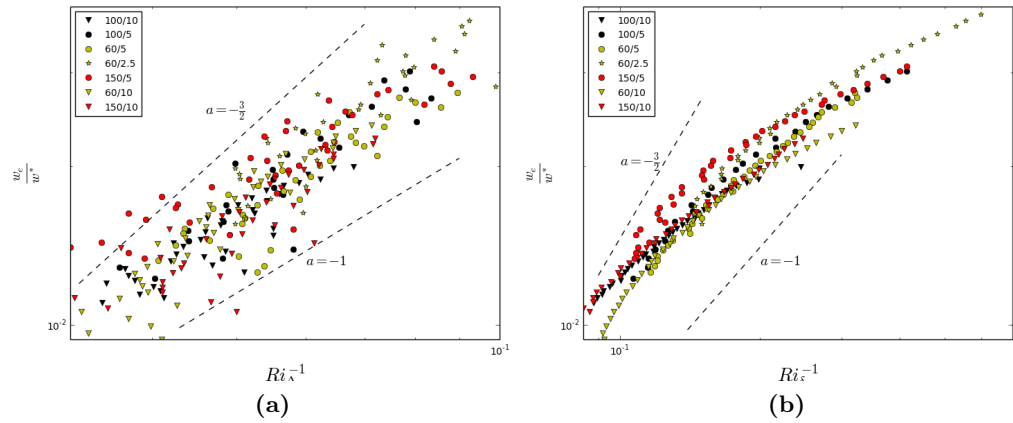


**Figure 2.43:** Scaled entrainment rate vs inverse Richardson number ( $Ri^{-1}$ ), where  $Ri$  is based on the  $\frac{\overline{w'\theta'}}{w'\theta'_s}$  profile using  $\Delta h$  accross the EL in (a) and  $\delta\theta$  at  $z_f$  in (b) (2.1)

## References

- Batchvarova, E. and S.-E. Gryning, 1994: An applied model for the height of the daytime mixed layer and the entrainment zone. *Boundary-Layer Meteorology*, **71**, 311–323.
- Betts, A. K., 1974: Reply to comment on the paper: "non-precipitating cumulous convection and its parametrization". *Quart. J. Roy. Meteor. Soc.*, **100**, 469 – 471.
- Boers, R., 1989: A parametrization of the depth of the entrainment zone. *Journal of Applied Meteorology*, 107–111.
- Brooks, I. M. and A. M. Fowler, 2012: An evaluation of boundary-layer depth, inversion and entrainment parameters by large-eddy simulation. *Boundary-Layer Meteorology*, **142**, 245–263.
- Crum, T. D., R. B. Stull, and E. W. Eloranta, 1987: Coincident lidar and aircraft observations of entrainment into thermals and mixed layers. *Journal of Climate and Applied Meteorology*, **26**, 774–788.
- Deardorff, J. W., 1970: Convective velocity and temperature scales for the unstable planetary boundary layer and for rayleigh convection. *Journal of the Atmospheric Sciences*, **27**, 1211 – 1213.
- Deardorff, J. W., 1972: Numerical investigation of neutral and unstable planetary boundary layers. *Journal of the Atmospheric Sciences*, **29**, 91 – 115.
- Deardorff, J. W., 1979: Prediction of convective mixed-layer entrainment for realistic capping inversion structure. *Journal of the Atmospheric Sciences*, **36**, 424–436.
- Deardorff, J. W., G. E. Willis, and B. J. Stockton, 1980: Laboratory studies of the entrainment zone of a convectively mixed layer. *J. Fluid Mech.*, **100**, 41–64.

- DuPont, E., J. Pelon, and C. Flamant, 1994: Study of the moist convective boundary layer structure by backscattering lidar. *Boundary Layer Meteorology*, **69**, 1 – 25.
- Federovich, E., R. Conzemus, and D. Mironov, 2004: Convective entrainment into a shear-free, linearly stratified atmosphere: Bulk models reevaluated through large eddy simulation. *Journal of the Atmospheric Sciences*, **61**, 281 – 295.
- Fedorovich, E. and R. Conzemius, 2001: *Large Eddy Simulation of Convective Entrainment in Linearly and Discretely Stratified Fluids*. 1st ed., Kluwer Academic Publishers.
- Garcia, J. R. and J. P. Mellado, 2014: The two-layer structure of the entrainment zone in the convective boundary layer. *Journal of the Atmospheric Sciences*, doi:10.1175/JAS-D-130148.1.
- Kolmogorov, A. N., 1962: A refinement of previous hypotheses concerning the local structure of turbulence in a viscous incompressible fluid at high Reynolds number. *Journal of Fluid Mechanics*, **13**, 82–85.
- Mahrt, L. and J. Paumier, 1984: Heat transport in the atmospheric boundary layer. *Journal of the Atmospheric Sciences*, **41**, 3061–3075.
- Nelson, E., R. Stull, and E. Eloranta, 1989: A prognostic relationship for entrainment zone thickness. *Journal of Applied Meteorology*, **28**, 885–901.
- Schmidt, H. and U. Schumann, 1989: Coherent structure of the convective boundary layer derived from large-eddy simulations. *J. Fluid Mech.*, **200**, 511–562.
- Sorbjan, Z., 1996: Effects caused by varying the strength of the capping inversion based on a large eddy simulation of the shear free convective boundary layer. *Journal of the Atmospheric Sciences*, **53**, 2015 – 2023.
- Sorbjan, Z., 1999: Similarity of scalar fields in the convective boundary layer. *Journal of the Atmospheric Sciences*, **56**, 2212 – 2221.
- Steyn, D. G., M. Baldi, and R. M. Hoff, 1999: The detection of mixed layer depth and entrainment zone thickness from lidar backscatter profiles. *Journal of Atmospheric and Oceanic Technology*, **16**, 953–959.
- Stull, R., 1973: Inversion rise model based on penetrative convection. *Journal of the Atmospheric Sciences*, **30**, 1092–1099.

Stull, R., 1988: *An Introduction to Boundary Layer Meteorology*. 1st ed., Kluwer Academic Publishers.

Sullivan, P. P., C.-H. Moeng, B. Stevens, D. H. Lenschow, and S. D. Mayor, 1998: Structure of the entrainment zone capping the convective atmospheric boundary layer. *Journal of the Atmospheric Sciences*, **55**, 3042–3063, doi:10.1007/s10546-011-9668-3.

Sullivan, P. P. and E. G. Patton, 2011: The effect of mesh resolution on convective boundary layer statistics and structures generated by large eddy simulation. *Journal of the Atmospheric Sciences*, **58**, 2395–2415, doi:10.1175/JAS-D-10-05010.1.

Tennekes, H., 1973: A model for the dynamics of the inversion above a convective boundary layer. *Journal of the Atmospheric Sciences*, **30**, 558–566.

Traumner, K., C. Kottmeier, U. Corsmeier, and A. Wieser, 2011: Convective boundary-layer entrainment: Short review and progress using doppler lidar. *Boundary-Layer Meteorology*, **141**, 369–391, doi:10.1007/s10546-011-9657-6.

Turner, J. S., 1986: Turbulent entrainment: the development of the entrainment assumption and its application to geophysical flows. *J. Fluid Mech.*, **173**, 431–471.

Vieth, E., 2011: Fitting piecewise linear regression functions to biological responses. *Journal of Applied Physiology*, **67**, 390–396.

# A. Appendices

## A.1 Potential Temperature: $\theta$

$$\theta = T \left( \frac{p_0}{p} \right)^{\frac{R_d}{c_p}} \quad (\text{A.1})$$

$p_0$  and  $P$  are a reference pressure and pressure respectively.

$$\frac{c_p}{\theta} \frac{d\theta}{dt} = \frac{c_p}{T} \frac{dT}{dt} - \frac{R_d}{p} \frac{dp}{dt} \quad (\text{A.2})$$

If changes in pressure are negligible compared to overall pressure, as in the case of that part atmosphere that extends from the surface to 2Km above it.

$$c_p \frac{d\theta}{\theta} = c_p \frac{dT}{T} - \frac{R_d}{p} \frac{dp}{p} \quad (\text{A.3})$$

$$\frac{d\theta}{\theta} = \frac{dT}{T} \quad (\text{A.4})$$

and if

$$\frac{\theta}{T} \approx 1 \quad (\text{A.5})$$

then small changes in temperature are approximated by small changes in potential temperature

$$d\theta \approx dT \text{ or } \theta' \approx T' \quad (\text{A.6})$$

and at constant pressure change in enthalpy (H) is

$$dH = c_p dT. \quad (\text{A.7})$$

## A.2 Second Law of Thermodynamics

$$\frac{ds}{dt} \geq \frac{q}{T} \quad (\text{A.8})$$

For a reversible process

$$\frac{ds}{dt} = \frac{q}{T} \quad (\text{A.9})$$

Using the first law and the equation of state for an ideal gas

$$\frac{q}{T} = \frac{1}{T} \left( \frac{dh}{dt} - \alpha \frac{dp}{dt} \right) = \frac{c_p}{T} \frac{dT}{dt} - \frac{R_d}{p} \frac{dp}{dt} \quad (\text{A.10})$$

so

$$\frac{ds}{dt} = \frac{q}{T} = \frac{c_p}{\theta} \frac{d\theta}{dt} \quad (\text{A.11})$$

For a dry adiabatic atmosphere

$$\frac{ds}{dt} = \frac{c_p}{\theta} \frac{d\theta}{dt} = 0 \quad (\text{A.12})$$

## A.3 Reynolds Decomposition and Simplification of Conservation of Enthalpy (or Entropy) for a dry Atmosphere

$$\frac{\partial \theta}{\partial t} + u_i \frac{\partial \theta}{\partial x_i} = \nu_\theta \frac{\partial^2 \theta}{\partial x_i^2} - \frac{1}{c_p} \frac{\partial Q^*}{\partial x_i} \quad (\text{A.13})$$

$\nu$  and  $Q^*$  are the thermal diffusivity and net radiation respectively. If we ignore these two effects then (adiabatic?)

$$\frac{\partial \theta}{\partial t} + u_i \frac{\partial \theta}{\partial x_i} = 0 \quad (\text{A.14})$$

$$\theta = \bar{\theta} + \theta', \theta = \bar{u}_i + u'_i \quad (\text{A.15})$$

$$\frac{\partial \bar{\theta}}{\partial t} + \frac{\partial \theta'}{\partial t} + \bar{u}_i \frac{\partial \bar{\theta}}{\partial x_i} + u'_i \frac{\partial \bar{\theta}}{\partial x_i} + \bar{u}_i \frac{\partial \theta'}{\partial x_i} + u'_i \frac{\partial \theta'}{\partial x_i} = 0 \quad (\text{A.16})$$

Averaging and getting rid of average variances and their linear products

$$\frac{\partial \bar{\theta}}{\partial t} + \bar{u}_i \frac{\partial \bar{\theta}}{\partial x_i} + u'_i \frac{\partial \theta'}{\partial x_i} = 0 \quad (\text{A.17})$$

Ignoring mean winds

$$\frac{\partial \bar{\theta}}{\partial t} + u'_i \frac{\partial \theta'}{\partial x_i} = 0 \quad (\text{A.18})$$

using flux form

$$\frac{\partial \bar{\theta}}{\partial t} + \frac{\partial (u'_i \theta')}{\partial x_i} - \theta' \frac{\partial u'_i}{\partial x_i} = 0 \quad (\text{A.19})$$

under the bousinesq assumption  $\Delta u_i = 0$

$$\frac{\partial \bar{\theta}}{\partial t} = - \frac{\partial (u'_i \theta')}{\partial z} \quad (\text{A.20})$$

ignoring horizontal fluxes

$$\frac{\partial \bar{\theta}}{\partial t} = - \frac{\partial (w' \theta')}{\partial z} \quad (\text{A.21})$$

#### A.4 Reynolds averaged Turbulence Kinetic Energy Equation

$$\frac{\partial \bar{e}}{\partial t} + \bar{U}_j \frac{\partial \bar{e}}{\partial x_j} = \delta_{i3} \frac{g}{\theta} \left( \bar{u}'_i \theta' \right) - \bar{u}'_i \bar{u}'_j \frac{\partial \bar{U}_i}{\partial x_j} - \frac{\partial \left( \bar{u}'_j e' \right)}{\partial x_j} - \frac{1}{\rho} \frac{\partial \left( \bar{u}'_i p' \right)}{\partial x_i} - \epsilon \quad (\text{A.22})$$

$e$  is turbulence kinetic energy (TKE).  $p$  is pressure.  $\rho$  is density.  $\epsilon$  is viscous dissipation.